



**Investigation of corium melt interaction with NPP reactor
vessel steel
(METCOR-P)**

**Progress report
01/07/08 –30/09/08**

INVESTIGATION OF MOLTEN UO_2 - ZRO_2 CORIUM INTERACTION
WITH NPP REACTOR VESSEL STEEL IN THE OXIDIZING
ATMOSPHERE ABOVE THE MELT

EXPERIMENT MCP-2

Project title	Investigation of Corium Melt Interaction with NPP Reactor Vessel Steel (METCOR-P) No. 3592	
Contracting organization	ISTC	
File code	RMP-02	
Project location	Alexandrov Research Institute of Technology of the RF Agency for Atomic Energy. NITI, Sosnovy Bor, 188540 Leningrad Region, Russia	
Project manager	Name	V.B. Khabensky
	Signature	
	Date	September, 2008

Authors

Dr.(Eng.), Prof.	V. B. Khabensky
Dr.(Eng.)	S. V. Bechta
Ph.D.	V. S. Granovsky
Ph.D.	A. A. Sulatsky
	S. A. Vitol
	E. V. Krushinov
Ph.D.	S. Yu. Kotova
Academician	V. V. Gusarov
Ph.D.	I. V. Kulagin
Ph.D.	D. B. Lopukh
	V. I. Almjashhev
	V. G. Bliznyuk
	V. R. Bulygin
	E. K. Kalyago
	N. E. Kamensky
	R.A. Kosarevsky
	A. V. Lysenko
	A. P. Martynov
	V. V. Martynov
	E. V. Shevchenko
	A. A. Chertkov
Ph.D.	S. A. Smirnov

ABSTRACT

The report presents a description and results of MCP-2 test of the ISTC METCOR-P Project No. 3592 carried out in the NITI, Sosnovy Bor, on the Rasplav-3 test facility.

Rates of corrosion have been determined for the NPP vessel steel interacting with molten $\text{UO}_2\text{-ZrO}_2$ corium in air, at a temperature on the steel specimen surface being within the 870...1370°C range. A correlation generalizing all experimental data for said corium composition has been proposed.

CONTENTS

INTRODUCTION	6
1. TEST DESCRIPTION	6
1.1. <i>Experimental facility diagram</i>	6
1.2. <i>Materials</i>	9
1.3. <i>Experimental procedure</i>	10
1.4 <i>Ultrasonic measurements of the specimen corrosion</i>	13
2. POSTTEST ANALYSIS	14
2.1 <i>Temperature condition of the specimen</i>	14
2.2 <i>Physicochemical analysis</i>	16
2.2.1 Ingot macrostructure	16
2.2.2 Material balance of the test	17
2.2.3 XRF of the witness specimen and fused products	18
2.2.4 Chemical analysis of the fused products	19
2.3 <i>SEM/EDX analysis</i>	21
3. DISCUSSION OF RESULTS	31
3.1 <i>Preliminary generalization of experimental data</i>	31
3.2 <i>Corrosion model</i>	33
3.3 <i>Experimental data generalization</i>	35
3.4 <i>The influence of the vessel steel corrosion at the interaction with corium on the IVR40</i>	
CONCLUSIONS	41
REFERENCES	42

INTRODUCTION

Experimental investigations of the interaction of NPP vessel steel with prototypic molten $\text{UO}_2\text{-ZrO}_2$ corium in steam (performed in the framework of the ISTC METCOR Project), have found the corrosion rate to differ from that during the interaction of steel with molten $\text{UO}_{2+x}\text{-ZrO}_2\text{-FeO}_y$ corium. However, the limited volume of experimental data on $\text{UO}_{2+x}\text{-ZrO}_2$ corium prevented reliable quantification of regularities.

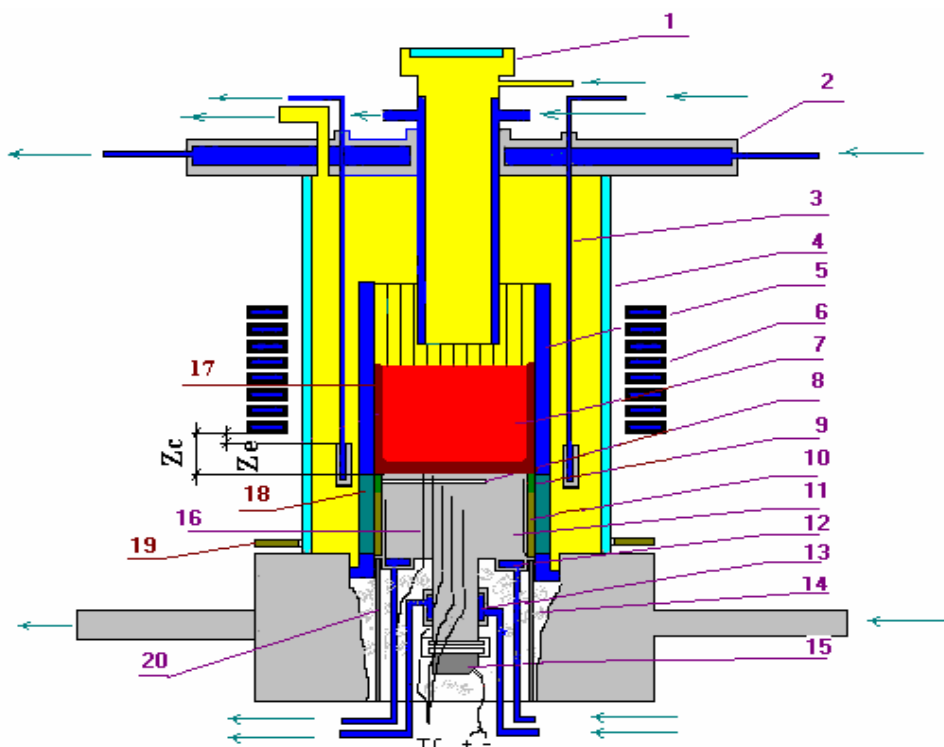
Therefore, MCP-2 was aimed at obtaining experimental data on the corrosion rate in the data-deficient domain of temperatures on the specimen surface, as well as at developing a model of corrosion and correlation that would generalize all experimental data on the NPP vessel steel corrosion in the oxidizing atmosphere above the melt of corium with said composition.

1. TEST DESCRIPTION

1.1. Experimental facility diagram

The test was carried out on the Rasplav-3 experimental facility. Before the test, the induction furnace power source had been modernized in order to increase power in the melt and maintain stability of the molten pool temperature. Two adjustment pretests have proved operability of the modernized facility. Diagram of the furnace is shown in Fig.1.1, where Z_c and Z_e – are coordinates of the specimen upper top and the cooled electromagnetic screen position relative to the inductor bottom end.

The vessel steel specimen is presented in Fig. 1.2. In order to evaluate heat fluxes from the melt to the specimen and for cooling the zone of the ultrasonic sensor coupling with the specimen, two calorimeters, the top and bottom ones, were provided.



1 – water-cooled pyrometer shaft; 2 – water-cooled cover; 3 – water-cooled electromagnetic screen; 4 – quartz tube; 5 – crucible section; 6 – inductor; 7 – melt; 8 – acoustic defect; 9 – fused ZrO_2 (fianite); 10 – powdered ZrO_2 ; 11 – vessel steel specimen; 12 –specimen top calorimeter; 13 – specimen bottom calorimeter; 14 – thermal insulation of mullite wool; 15 –US sensor; 16 – K-type thermocouples; 17 – crust, 18 – electromagnetic screen (interwelded crucible sections); 19 – non-cooled electromagnetic screen; 20 – specimen cylindrical support

Fig. 1.1 – Furnace schematics

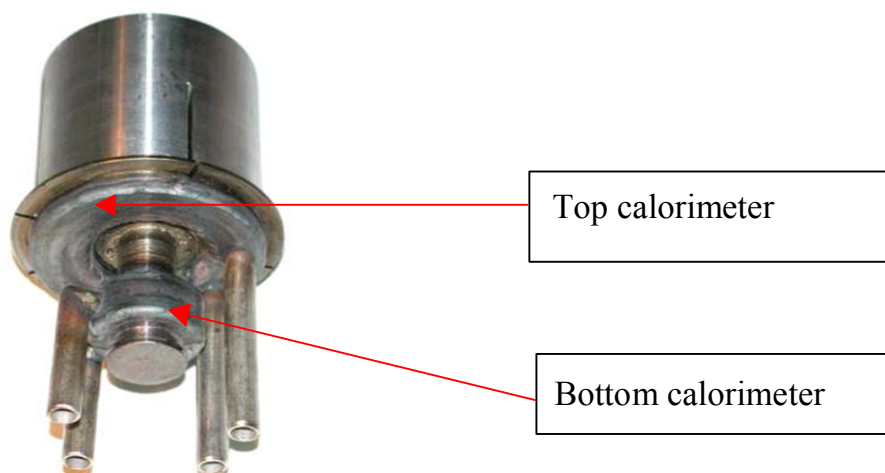


Fig. 1.2 – Vessel steel specimen

Fig.1.3 and Tab. 1.1 give the locations of K-type thermocouple junctions in the specimen. Within a 10 mm radius from the specimen axis, the thermocouples were embedded into channels \varnothing 1.5 mm, and within a 29 mm radius – into the 1.5 mm-wide carved grooves. To control the corrosion front position more accurately by means of ultrasonic sounding, an acoustic defect representing a channel \varnothing 2 mm was drilled in the specimen perpendicular to the axis.

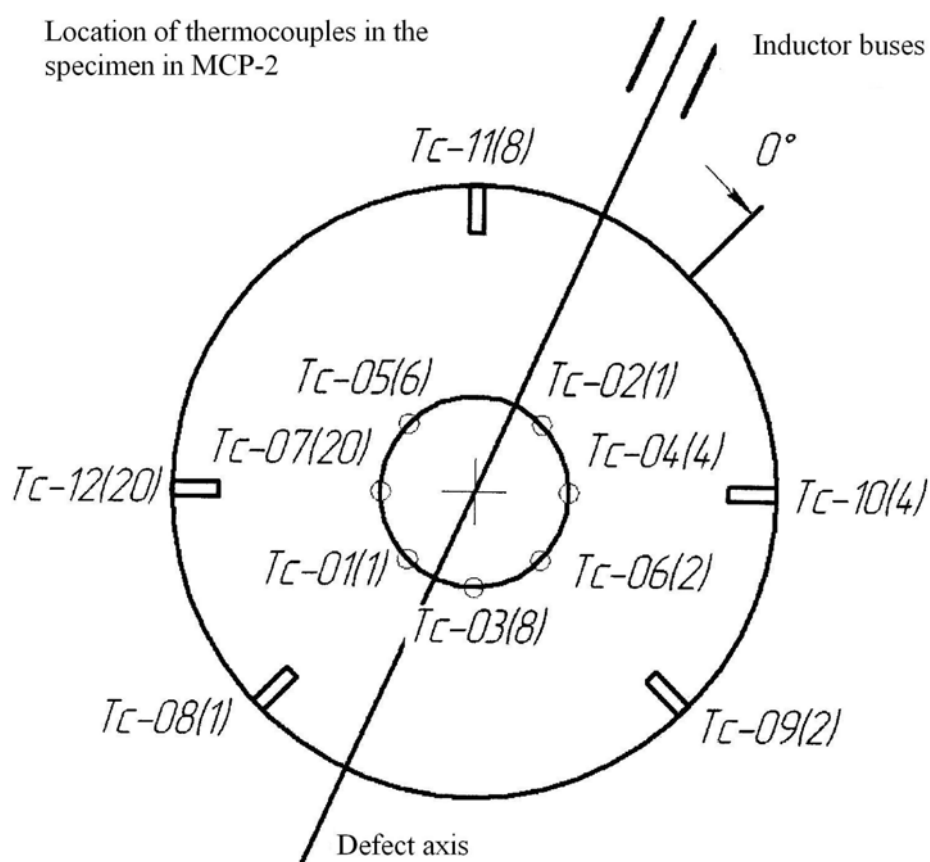


Fig. 1.3 – Thermocouple hot junction locations

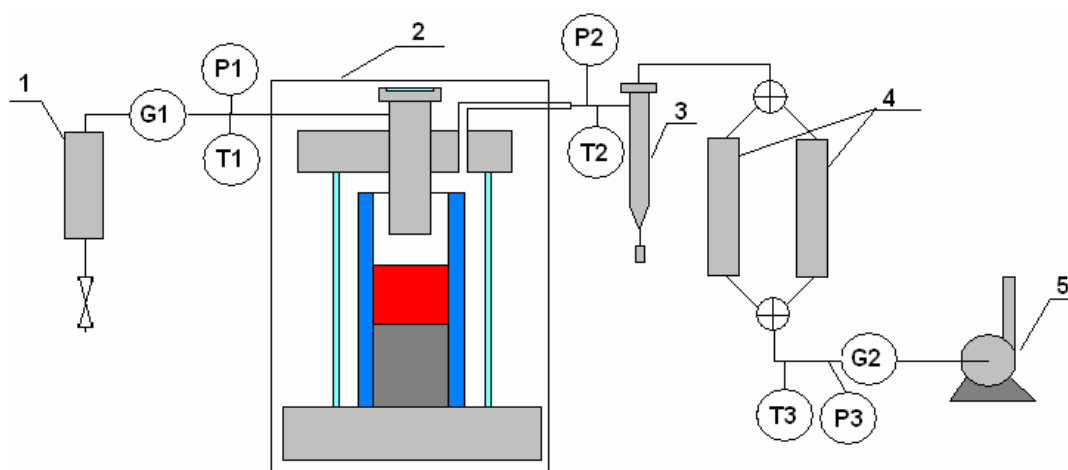
Table 1.1**Thermocouple hot junction locations**

No.	α° (horizontal angle)	r, mm (distance from the specimen axis to the hot junction)	h, mm (distance from the specimen upper surface to the hot junction)
Tc-01	180	10	0.5
Tc-02	0	10	0.8
Tc-03	135	10	8
Tc-04	45	10	3.5
Tc-05	270	10	6
Tc-06	90	10	2.2
Tc-07	225	10	20.8
Tc-08	180	29	1
Tc-09	90	29	2
Tc-10	45	29	4
Tc-11	315	29	8
Tc-12	225	29	20
USS	45	7.5	104.3

To avoid electromagnetic heating of the specimen, gaps between crucible sections in the lower zone of specimen location were solid welded to produce an electromagnetic screen (18). The specimen was placed in the crucible in such a way that its top was 1 mm below the top of said electromagnetic screen. The gap between the specimen and crucible sections was filled with powdered ZrO₂ (10) and particles of fused stabilized ZrO₂ (9). Additional screening of the specimen from induction heating and adjustment of crust thickness on the specimen surface were provided by the water-cooled movable screen (3). The melt surface monitoring and temperature measurements were carried out via the water-cooled air-purged pyrometer shaft (1).

To measure the distance from the corrosion front to the acoustic defect (8), the same ultrasonic sensor (15) as the one used in the MC experimental series [1] was used.

To supply air into the furnace and ventilate it, a gas-aerosol system has been assembled. Its diagram is presented in Fig. 1.4. The air flow through the furnace was ensured by the vacuum pump (5). A silica gel column (1) was applied for removing moisture from air at the furnace inlet. To clean gases from aerosols, the cyclone (3) and the switched in turn Large Area Filters (4) were employed. To control the gas flow parameters (flow rate, pressure and temperature), electromechanical flow meters G1, G2 of the OP-40/C type, Motorola pressure transducers P1,2,3 and L-type thermocouples were installed in places marked by dots in the diagram.



1 – silica gel dehumidifier; 2 – furnace; 3 – cyclone;
4 – Large Area Filter (LAF); 5 – vacuum pump; P1-P3 – pressure transducers;
G1,2– flow rate transducers; T1-T3 – thermocouples.

Fig.1.4 – Gas and aerosols in and out diagram

1.2. Materials

The materials used in the test included 15Kh2NMFA-A vessel steel, urania, zirconia and metallic zirconium. All oxides and metallic zirconium have been checked for the main substance content. In addition, the powdered urania was checked by thermogravimetry and the oxygen/uranium ratio was found to equal 2.24 for the powder and 2.0 for the ground fuel pellets. The composition of corium charge is given in Tab. 1.2.

Table 1.2

Charge components composition

Component	Main substance content, %	Impurities, mass %	Note
Powdered $\text{UO}_{2.24}$, <100 μm dispersivity	>99.9	Fe < 0.03; As < 0.0003; Cu < 0.01; phosphates <0.002; chlorides < 0.003	Certificate data; thermogravimetry
Ground UO_2 fuel pellets, <2 mm dispersivity	>99.0	Fe<0.03; As<0.0003; CuO<0.01; phosphates <0.002; chlorides <0.003.	Certificate data; thermogravimetry
ZrO_2	($\text{ZrO}_2 + \text{HfO}_2$) > 99.4	Al_2O_3 < 0.03; Fe_2O_3 < 0.05; CaO < 0.03; MgO < 0.02; SiO_2 < 0.2; TiO_2 < 0.1; P_2O_5 < 0.15; ($\text{Na}_2\text{O} + \text{K}_2\text{O}$) < 0.02	Certificate data
Zr, Nb -1 alloy	Zr>99.0	Nb < 1.0	XRF

The masses of components loaded into the crucible before melting are given in Tab. 1.3

Table 1.3

Charge components composition and masses

Purpose	Component	Fraction, μm	Mass, g
Crust imitator	Corium from Pr2-MCP-2 ¹⁾	< 50	153.3
Main charge	Corium from Pr2-MCP-2 ¹⁾	<500	1451.2
	UO ₂	< 100	67.2
	Metallic zirconium as the start-up material, Zr	Rods \varnothing 3 mm and 15 mm long	20.3
Total:			1692.0

¹⁾ – composition determined by XRF and chemical analysis is offered in Tab. 2.3.

The crucible was charged with a corium composed of 71.0% UO_{2+x} + 29.0% ZrO₂ (mass % here and further in the text) fused in air in the specially conducted Pr2-MCP-2 pretest. The loading procedure was as follows: a layer of crust imitator, with particles dispersivity below 50 μm and composition corresponding to the equilibrium melt composition in air, was placed on the steel specimen top, and above it followed a mixture of the imitator (300-500 μm dispersivity) with powdered UO₂. Metallic Zr was used as the start-up material.

1.3. Experimental procedure

The start-up heating and molten pool formation in air were done at $Z_c=20$ mm, $Z_e=10$ mm, where Z_e , Z_c – are distances from the inductor bottom end to the electromagnetic screen and to the welded sections upper edge, respectively (Fig.1.1).

In order to decrease thermal losses of the melt via radiation, a crust was formed at the pool surface. To stabilize the specimen surface temperature, the screen was lifted for 3 mm ($Z_c=20$ mm, $Z_e=7$ mm) at 1498 s. By 2000 s the specimen top temperature has reached about 850°C and according to the test plan, from that moment investigation of the vessel steel corrosion kinetics at the interaction with corium through the crust in air was initiated during the 1st regime of the specimen stabilized temperature. At 9317 s, the crust on the pool surface was broken through and melt sampled.

At 10500 s transition to the 2nd specimen temperature regime was made. At this time, the screen was lowered for 4.5 mm ($Z_c=20$ mm, $Z_e=11.5$ mm). The specimen top temperature reached about 950°C, and from 11000 s through 15100 s the 2nd regime of temperature stabilization was investigated. In order to compensate for the melt lost through evaporation, 50 g of urania were introduced into the melt at 14791 s.

At 15167 s, transition to the 3rd specimen temperature regime was made. At this time, the screen was lowered for 3 mm ($Z_c=20$ mm, $Z_e=14.5$ mm). The specimen top temperature was about 1100°C and the 3rd regime continued from 15500 through 16370 s.

At 16378 s, transition to the 4th specimen temperature regime was made. At that, the power in the melt was increased. The specimen top temperature amounted to approximately 1150°C and the 4th regime lasted from 16500 s through 18300 s.

Corrosion rate was increasing as the specimen temperature kept growing. Therefore, the subsequent regimes were comparatively short and temperature stabilization of the specimen was, as a rule, not achieved during these regimes.

As with the transition to the 4th regime, power in the melt was increased when transiting to all other regimes.

The 5th regime continued approximately from 18530 s through 19340 s, the 6th – from 19340 s through 20000 s, the 7th – from 20000 s through 20640 s, the 8th – from 20640 s through 21210 s, the 9th – from 21210 s through 21920 s. The specimen top temperature was continuously growing during these regimes from about 1200 up to 1350°C.

At 21953 s of the test heating was switched off and the ingot with specimen were cooled down in air.

Figs. 1.5 – 1.9 offer the results of temperature, electric parameters, thermal and electrical power measurements in MCP-2.

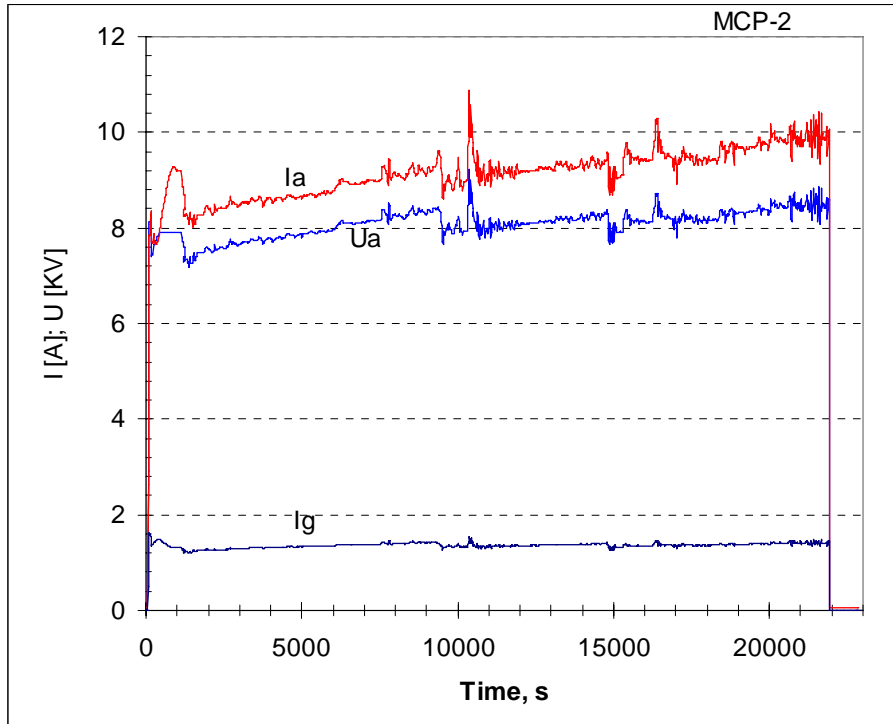
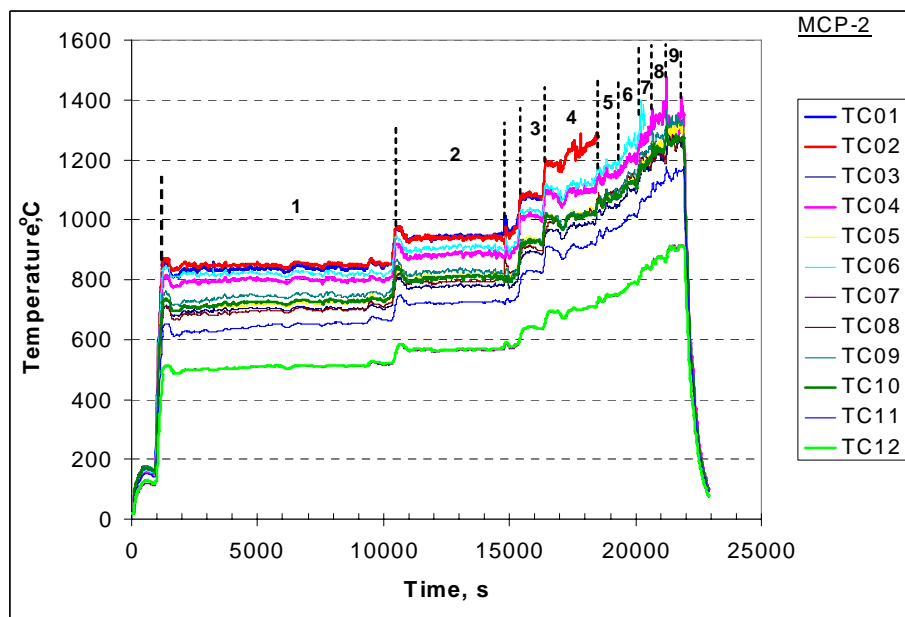


Fig. 1.5 – History of anode current (Ia), voltage (Ua) and grid current (Ig) of the generator valve.



1-9 – Regime numbers; - - - - - temporal boundaries of regimes

Fig. 1.6 – Thermocouple readings in MCP-2

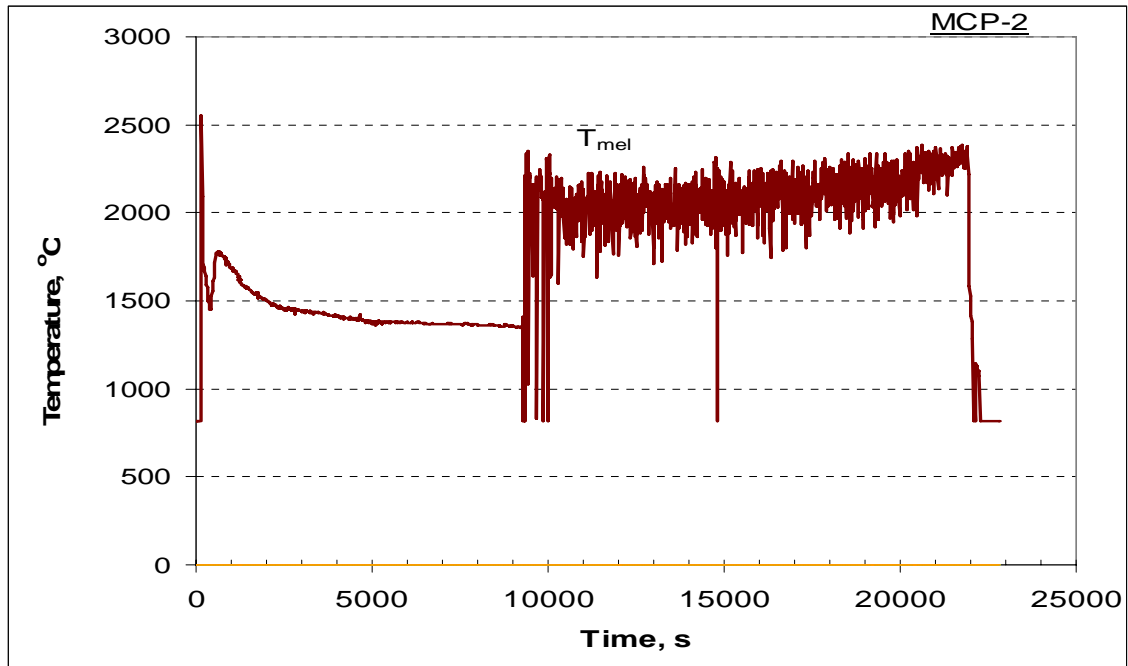
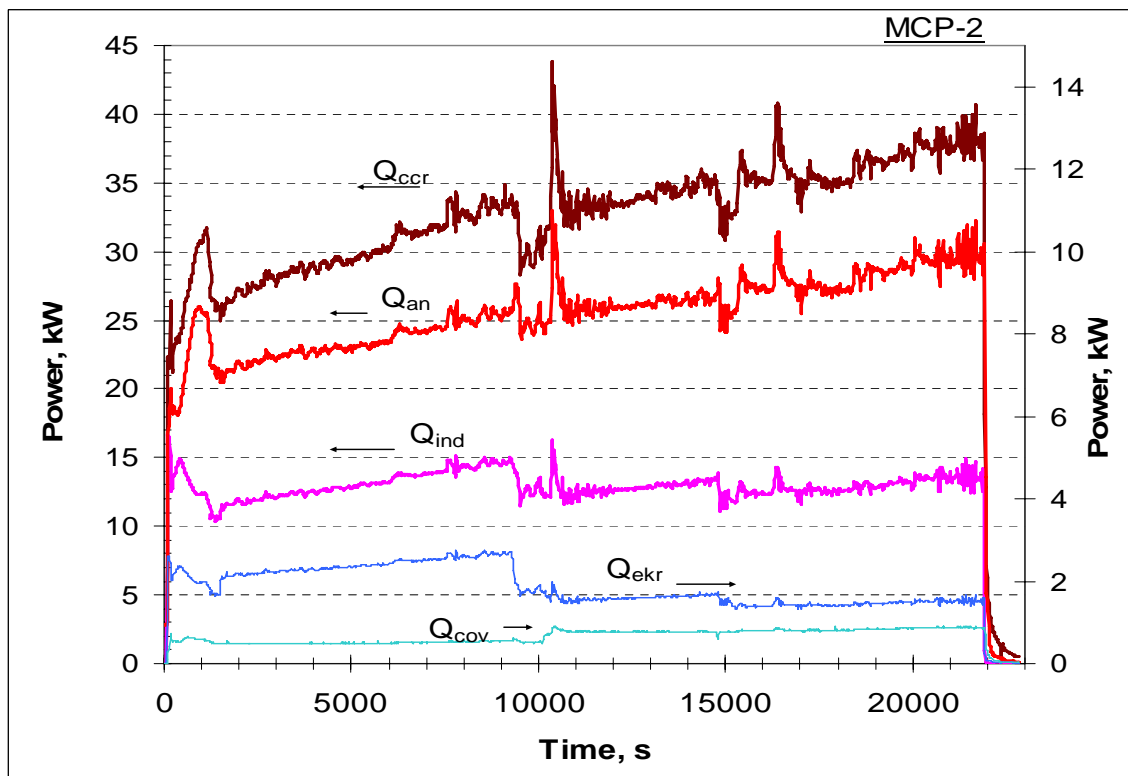


Fig. 1.7 – Pyrometer readings in MCP-2



Q_{ccr} – electrical and thermal losses in the crucible; Q_{ind} – electrical losses in the inductor; Q_{ekr} – electrical losses in the electromagnetic screen; Q_{cov} – electrical and thermal losses in the cover; Q_{an} – electrical losses in the anode of the HF generator valve.

Fig. 1.8 – Power extracted by cooling water from the furnace elements and generator

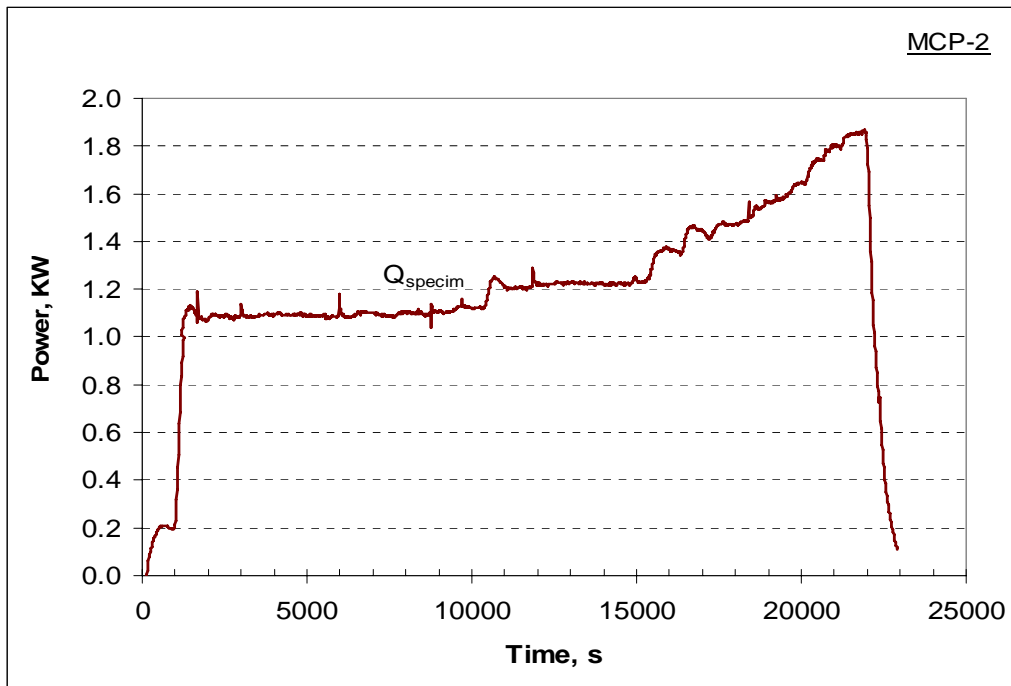


Fig. 1.9 – History of thermal power Q_{specim} , into the upper calorimeter

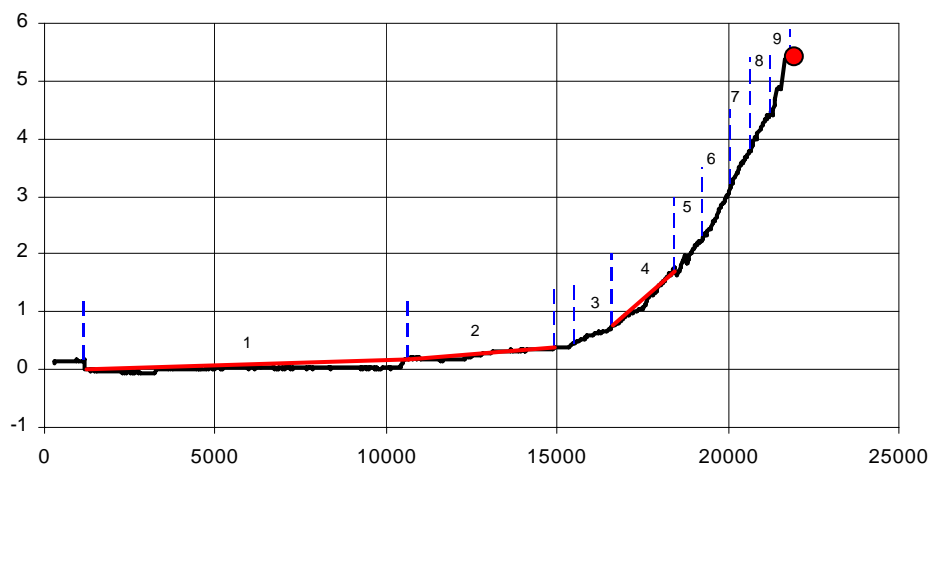
1.4 Ultrasonic measurements of the specimen corrosion

The technique of specimen corrosion depth measurement in MCP-2 did not differ from that applied in MC10 and MC11 [1].

Fig. 1.10 shows the results of online measurements. Like in MC12 [2], the measurements made during the initial instants of a regime were regarded as reliable for a number of regimes, especially at a relatively low temperature on the specimen top, and corrosion rate was calculated from the obtained difference and duration of the regime. In Fig. 1.10 these areas are shown as linear sections.

The sufficient precision of US measurements may be judged from the fact that the corrosion depth registered by the end of the test practically coincided with the value of about 5.5 mm (in the USS sighting spot $\varnothing 15$ mm) obtained from the profilogram in Fig. 2.4.

h, mm



t, s

1÷9 – Regime numbers; - - - - temporal boundaries of regimes; • – posttest measurement
Fig. 1.10 – Kinetics of the steel specimen corrosion in the ultrasonic sensor sighting spot

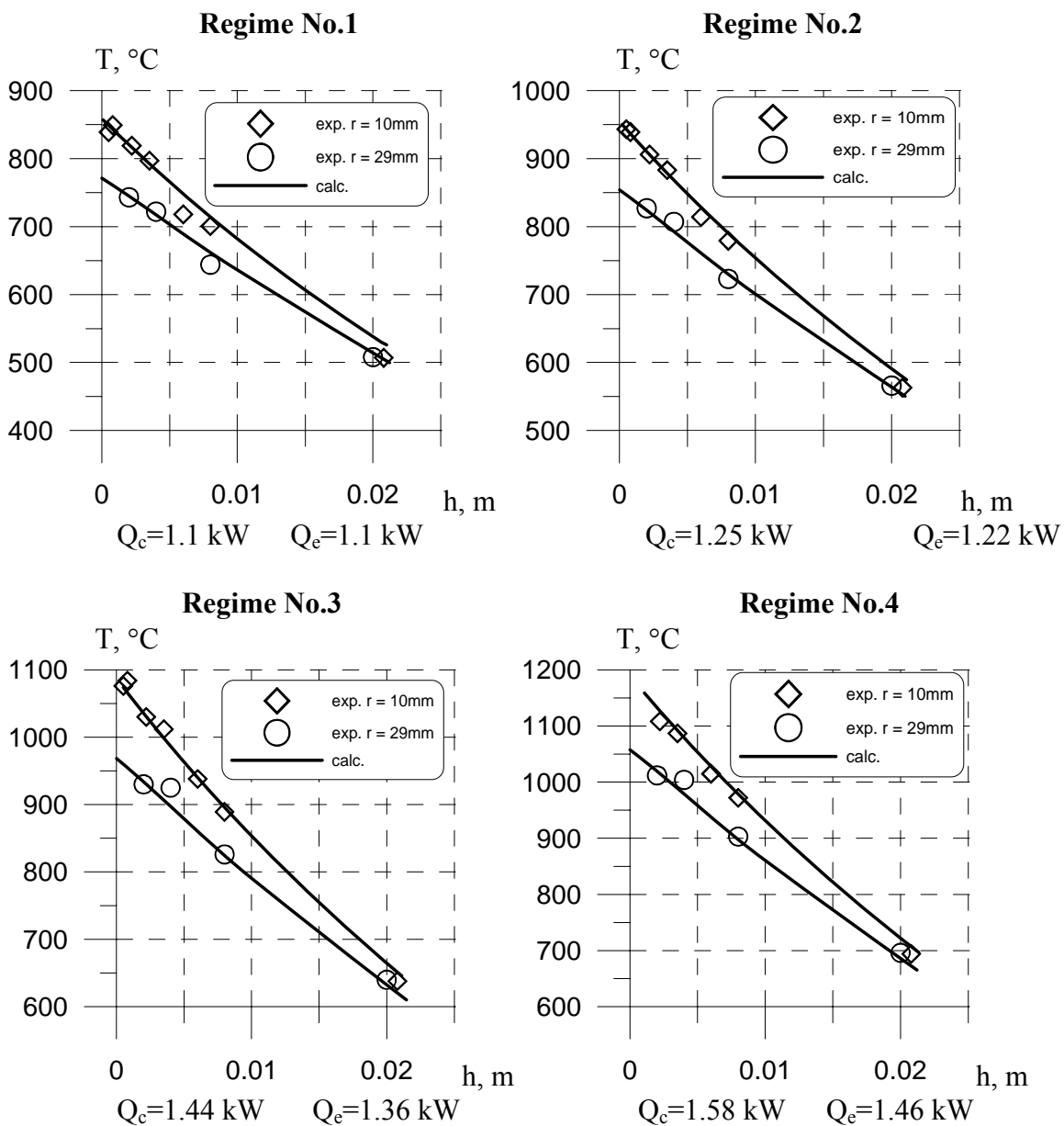
2. POSTTEST ANALYSIS

2.1 Temperature condition of the specimen

The temperature and heat flux at the specimen top in the US sensor sighting spot have been calculated for each of the 9 regimes. The calculation technique is given in [1]. The results of calculations for regime No.2 in MC10 [1], in which corium of the same composition as in MCP-2 was interacting with the specimen, were approximately accepted for heat flux distribution along the specimen top radius.

Corrosion was changing the specimen top surface position and shape, so these data for calculations were taken for the middle of each regime time interval and determined by the US measurements. Thermocouple measurements for each regime have been time averaged.

Precision of the specimen temperature condition numerical modeling and, therefore, of determining the required temperature and heat flux at the interaction interface may be judged by comparing the calculated values and thermocouple readings given in Fig. 2.1.



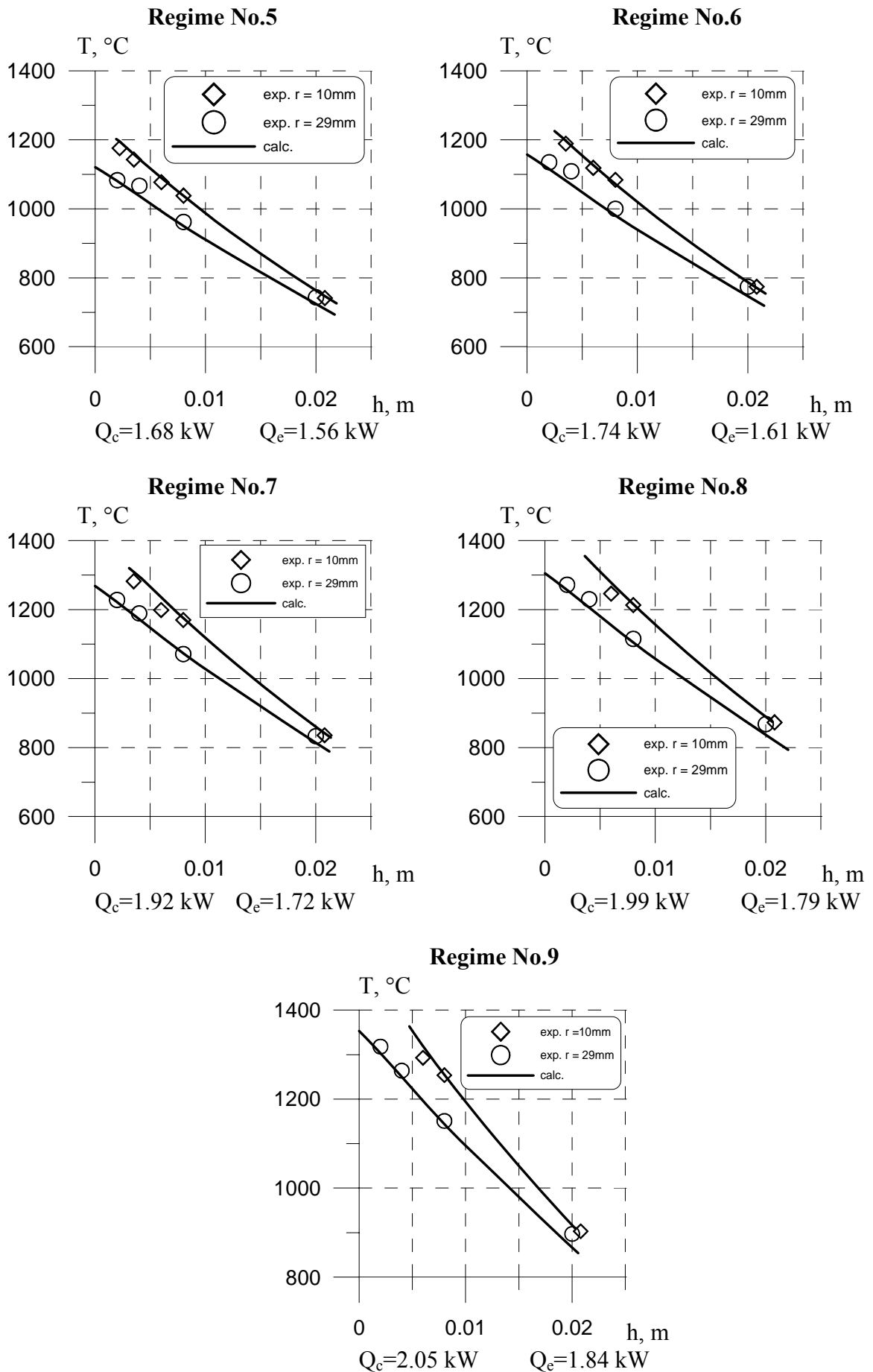


Fig. 2.1 – Temperature distribution along the specimen height during different regimes

Also, Fig. 2.1 offers the calculated values of Q_c and experimentally determined values of thermal power (Q_e) from the specimen into the top calorimeter, the discrepancy of which does not exceed 10%. The readings of TC-08 thermocouple were disregarded due to the systematic temperature underrating. The readings of TC-01, TC-02, TC-04, TC-06 were also disregarded after their hot junctions had been reached by the corrosion front, as due to destruction the readings could be incorrect.

Tab. 2.1 offers the calculated temperatures and heat fluxes at the specimen surface, and the corresponding corrosion rates for all regimes (averaged, in the USS sighting spot).

Table 2.1

MCP-2 results			
Regime No.	Steel surface temperature, °C	Heat flux, MW/m²	Corrosion rate, mm/h
1	870	0.74	0.085
2	950	0.81	0.13
3	1080	0.92	0.7
4	1165	1.0	1.77
5	1210	1.04	2.38
6	1230	1.06	3.46
7	1325	1.15	4.25
8	1350	1.17	4.75
9	1370	1.19	5.8

2.2 Physicochemical analysis

2.2.1 Ingot macrostructure

When disassembling the furnace after MCP-2, crucible sections were found to be coated with aerosols (see Fig. 2.2). During the corium ingot and steel specimen extraction from the crucible, the former separated from the steel specimen and destroyed. A part of the oxidic ingot was later reconstructed and oxidic ingot fragment/steel specimen relative position determined (see Fig. 2.3). The oxidic ingot fragment and steel specimen were separately embedded into epoxy, and templates for the SEM/EDX were prepared from them.

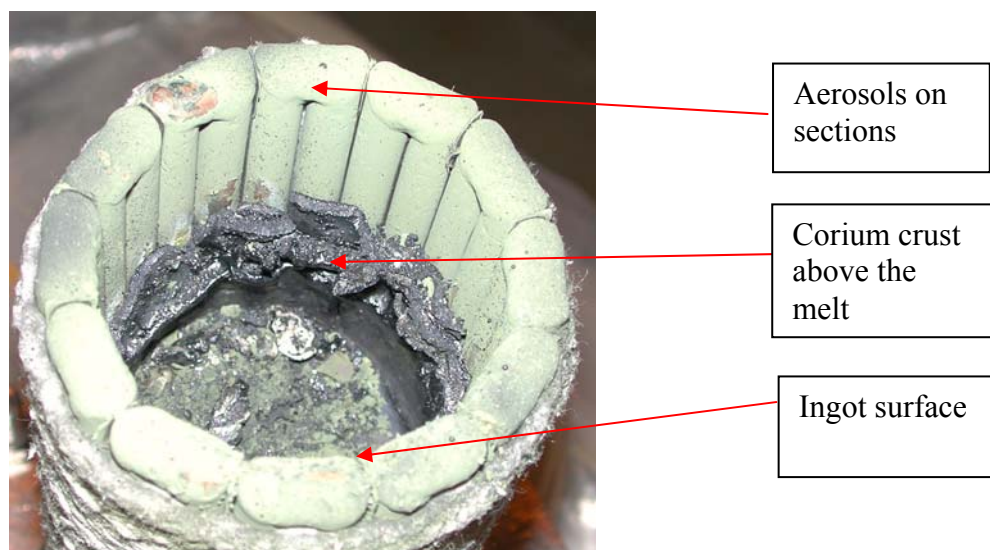


Fig. 2.2 – The crucible with ingot before furnace disassembly

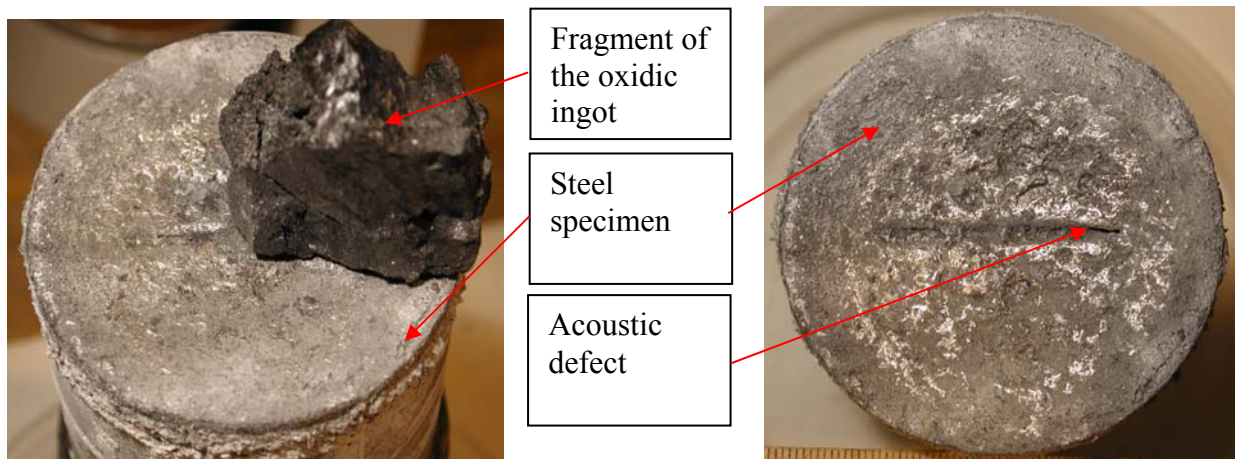


Fig. 2.3 – Fragment of the oxidic ingot adjacent to the specimen, and the steel specimen surface from the corium-facing side after the test

Fig. 2.4 shows a photograph of the specimen top part longitudinal section and the surface profilogram along this section. The maximum depth of corrosion (along the specimen axis) was 5.45 mm.

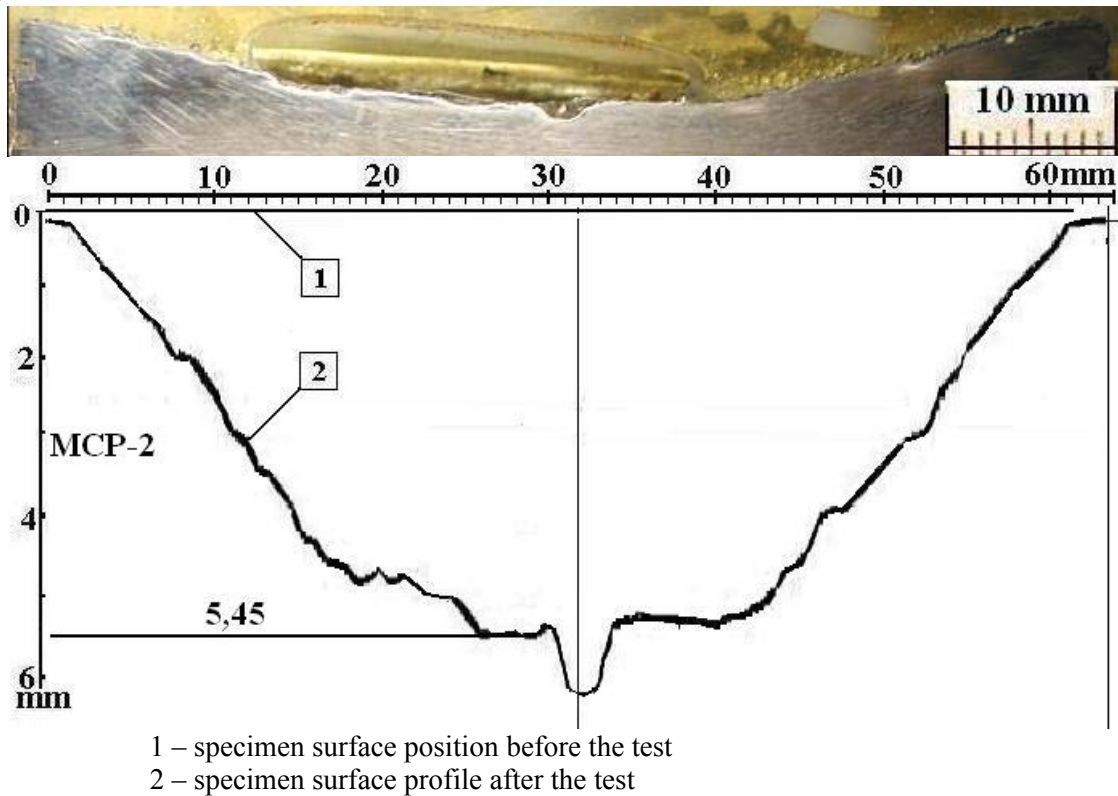


Fig. 2.4 – Specimen longitudinal section and profilogram

2.2.2 Material balance of the test

In order to make the material balance, the initial charge components and fused products were weighed with accuracy up to 0.1 g and then analyzed for the content of main components.

Material balance for MCP-2 is given in Tab. 2.2.

Table 2.2

Material balance of corium components in MCP-2

Introduced into the melt, g		Collected after the test, g	
UO ₂	67.2	Ingot	1408.8
Zr	20.3	Aerosols	59.4
Crust ²⁾	153.3	Spillages ¹⁾	137.8
Ingot from Pr2-MCP-2 ³⁾	1451.2	Rod sample	6.5
ZrO ₂ (fused)	38.8	Above-melt crust	297.0
ZrO ₂ (fine-dispersed)	60.6		
Added UO ₂	50.0		
Σ	1841.4	Σ	1909.5
Debalance	+68.1		

¹⁾ – The spillages include: charge material, ZrO₂ (fine-dispersed) and fused ZrO₂ from thermal insulation;

²⁾ – The corium fused in air in Pr2-MCP-2 pretest was used as the crust;

³⁾ –Composition of the ingot from Pr2-MCP-2 according to physicochemical analysis is given in Tab. 2.3.

Tab. 2.2 clearly shows that the debalance value is +68.1 g. The increment in mass is firstly determined by transition of some iron from the steel specimen into molten corium (the specimen has corroded up to the acoustic defect - see Fig. 2.3) and, secondly, due to oxidation of metallic Zr (the start-up material) and of a part of urania (up to UO_{2+x}) by oxygen in air.

Tab. 2.3 offers the results of physicochemical analysis of an average samples from the ingot from Pr2-MCP-2. Since the applied analytical methods (XRF, chemical analysis) were not used for direct measurements of oxygen, in Tab. 2.3 and further in Tab. 2.5, 2.6 it was determined from the residue. The corium fused in Pr2-MCP-2 pretest (153.3 g, >50 μ m dispersivity) was used as the crust imitator. The corium that left from Pr2-MCP-2 was crushed down into 300 – 500 μ m-sized particles and used in MCP-2 as the charge material. The data from Tab. 2.3 were used for composing the per-element mass balance (see Tab. 2.5).

Table 2.3

Physicochemical analysis of an ingot average sample from Pr2-MCP-2

Element	XRF	Chemical analysis
	mass %	
U	61.87	62.10
Zr	21.40	21.20
Impurities and O ¹⁾	16.73	16.70

¹⁾ – impurities and oxygen determined from residue

2.2.3 XRF of the witness specimen and fused products

The elemental composition of the witness specimen and fused products was determined by XRF using the SPECTROSCAN MAX-GV spectrometer.

The vessel steel witness specimen, a \varnothing 40 mm disk, was lathed from the specimen cylindrical blank and subjected to XRF.

Tab. 2.4 contains the results of the vessel steel witness specimen analysis compared with Specifications for this grade of vessel steel.

Table 2.4**XRF results for the vessel steel witness specimen**

Specs., analytical method	Content, mass %											
	C	Si	Mn	Cr	Ni	Mo	V	P	S	Cu	Co	As
Specs. 108-765-78	0.13-0.18	0.17-0.37	0.30-0.60	1.8-2.3	1.0-1.5	0.5-0.7	0.10-0.12	<0.02	<0.02	<0.3	<0.03	<0.003
XRF	-	0.25	0.49	2.24	1.00	0.70	0.10	<0.02	-	0.07	<0.03	<0.003

The XRF results confirm the compliance of the steel used in the test to Specifications 108-765-78.

Upon completing MCP-2 a fragment of corium ingot (see Fig.2.3) together with the steel specimen were embedded in epoxy and cut along the axis. The remaining corium ingot, above-melt crust and rod sample were crushed into particles smaller than 3 mm. Then an average ingot samples were taken by quartering, ground into particles sized less than 50 μm and subjected to XRF and chemical analyses for determining their composition.

Since XRF is capable of providing the most comprehensive per-element analysis, this method was used for checking material balance for MCP-2 (for results, see Tab. 2.5).

The mass of aerosol deposits on the MAF and LAF was determined by gravimetry using the VLR-200G laboratory equal-arm balance of the 2nd class. The accuracy of weighing was ± 0.12 mg. A special technique employing exposure in the exiccator with concentrated sulfuric acid was developed for both preparing the filters for the test and measuring the sample weights.

The mass balance made for MCP-2 (Tab. 2.5) shows that the debalance for the main elements, that is uranium (-0.2 g) and zirconium (-3.9 g) is less than 1 percent of the introduced amount and can mainly be explained by the analytical error, which amounts to 5 relative % for U and Zr. The oxygen debalance amounted to +6 g and was due to metallic zirconium (the start-up material), iron and urania by oxygen in air.

According to the profilogram (see Fig. 2.4) the amount of iron that oxidized and transited into molten corium was calculated to be 57.7 g – based on the calculated volume of oxidized steel that transited into the melt ($\sim 7.34 \text{ cm}^3$) and its density of $\sim 7.87 \text{ g/cm}^3$. Practically, the calculated mass coincides with that of iron in corium obtained by XRF, i.e. 58.0 g, (Tab. 2.5).

2.2.4 Chemical analysis of the fused products

The melt sample taken using the rod (rod sample), the above-melt crust, ingot and aerosols were crushed down to 100 μm particles, quartered, further crushed to particles not exceeding 50 μm and examined for the content of U, Zr and Fe.

Corium samples were analyzed applying the previously elaborated technique [1], the essence of which is in taking a 0.1 g sample weight of ground corium, dissolving it in a mixture of concentrated orthophosphoric and sulphuric acids (1:2) in flowing argon, and then determining the content of Fe^{2+} and Fe^{3+} by photolorimetry with orthophenanthroline, and that of U^{4+} and U^{6+} – using arsenazo III [3-5].

Besides, samples preparation employed the technique of fusing 0.1 - 0.5 g samples from the ingot and other fused products with 3.0 ± 0.5 g of potassium pyrosulphate at $900 \pm 25^\circ\text{C}$ until the appearance of a transparent alloy, which was further dissolved at heating it in 200...250 ml 1M solution of sulphuric acid. Then zirconium was determined as Zr^{4+} by photometry with orange xylenol, total U with arsenazo III, and Fe with orthophenanthroline. Free zirconium (Zr_{free}) was determined by volumetry.

Table 2.5

XRF data for samples from MCP-2 and per-element mass balance for the test

Sample	U	Zr	Fe	Cr	Ni	Mn	O ³⁾	Mass, g	U	Zr	Fe	Cr	Ni	Mn	O ³⁾
	mass %								g						
Ingot (corium average sample)	58.7	21.5	3.9	0.1	0.04	0.03	15.73	1408.8	827.0	302.9	54.943	1.409	0.564	0.423	221.6
Spillages	63.7	19.9	-	-	-	-	16.40	38.4	24.4	7.7	-	-	-	-	6.3
Molten corium sample	61.6	22.3	<0.05	-	-	-	16.05	6.5	4.0	1.4	0.003	-	-	-	1.0
Above-melt crust	64.6	18.6	0.2	-	-	-	16.60	297.0	191.9	55.2	0.594	-	-	-	49.3
Aerosols from cyclone Point.3 ¹⁾	82.2	0.278	0.2	-	-	-	17.32	3.2	2.7	0.0	0.006	-	-	-	0.6
Aerosols from quartz tube, Point.5 ²⁾	82.7	0.774	<0.05	-	-	-	16.48	24.7 ⁴⁾	20.4	0.2	0.012	-	-	-	4.1
Aerosols from MAF1	81.5	0.202	<0.05	0.04	0.02	0.06	18.13	5.5	4.5	0.0	0.003	0.002	0.001	0.003	1.0
Aerosols from LAF1	83.1	0.21	<0.05	-	-	-	16.64	12.8 ⁵⁾	10.6	0.0	0.006	-	-	-	2.1
Aerosols from LAF2	81.4	0.191	<0.05	-	-	-	18.36	13.2	10.8	0.0	0.007	-	-	-	2.4
Collected in the end of the test								1810.1	1096.2	367.5	55.6	1.4	0.6	0.4	288.4
Introduced into the melt								1742.0	1096.0	363.6	-	-	-	-	282.4
Δ								+68.1	-0.2	-3.9	+55.6	+1.4	+0.6	+0.4	+6.0

¹⁾ see Fig.1.3; ²⁾ see Fig.1.1; ³⁾ O and impurities determined from residue; ⁴⁾ The mass of aerosols collected from the quartz tube includes masses of those collected from the water-cooled pyrometer shaft (see Fig.1.1, Point 3) and in transport lines (see Fig.1.3); ⁵⁾ The mass of aerosols collected from LAF1 includes the mass of those collected from MAF2, which haven't been analyzed due to their small quantity:: LAF1 - 12.3 g, MAF2 - 0.5 g.

The method of total Zr determination is based on the formation of a colored complex compound of Zr (IV) and orange xylenol in the sulphuric acid solution with molar concentration of the equivalent of 0.3 – 0.4 mole/dm³ [6-8]. The evaluation of zirconium is not complicated by large quantities of Mo, W, U, Zn and Ti, as well as impurities of Fe (up to 50 µg), Pb, Ni, Cu, Th and Ta (>100 µg) [7-8].

The results of chemical analysis of samples are presented in Tab. 2.6.

Table 2.6

Sample	Content, mass %					
	Fe ²⁺	Fe ³⁺	U ⁴⁺	U ⁶⁺	Σ Zr	Impurities and O ³⁾
Ingot (corium average sample)	3.2	2.2	49.3	7.7	21.7	15.9
Above-melt crust	1.0	n/found	46.2	15.1	19.0	18.7
Molten corium sample	n/found	n/found	48.7	12.3	23.5	15.5
Aerosols from cyclone, Point 3¹⁾	0.7	n/found	31.0	52.0	n/determ.	16.3
Aerosols from quartz tube, Point 5²⁾	0.3	n/found	30.0	52.4	n/determ.	17.3
Aerosols from MAF1	n/found	n/found	30.0	52.6	n/determ.	17.4
Aerosols from LAF1	n/found	n/found	29.2	53.3	n/determ.	17.5
Aerosols from LAF2	n/found	n/found	29.3	52.7	n/determ.	18.0

¹⁾ see Fig.1.3;

²⁾ see Fig.1.1;

³⁾ O and impurities determined from residue.

The error of U content determination by photolorimetry did not exceed 5 relative %, and that of Zr and Fe determination was not above 3 relative %.

A comparison of the XRF (Tabs. 2.5) and chemical analysis (Tab. 2.6) results concerning the main components in the samples has shown them to be in satisfactory accord.

Physicochemical analysis has shown a part of steel components to transit into molten corium at the interaction of corium with steel specimen (see Tabs. 2.5, 2.6) and oxidize.

2.3 SEM/EDX analysis

Two polished sections for SEM/EDX were produced from a half of the steel specimen longitudinal section and a quarter of the ingot oxidic part longitudinal section (Fig. 2.5). Visual examination of the polished sections makes it possible to make a statement about the absence of macrostructural inhomogeneity in both sections. A rough boundary of the degraded steel should be noted, however, as it may speak of inaccessibility of the stationary status by the system. SEM/EDX was used to investigate the steel/corium interaction zone (Fig. 2.5, zones 1-14) and the crystallized corium in proximity to the interaction zone (Fig. 2.5, zones 15-21).

EDX results for steel composition in different parts of the polished sections (Tab. 2.7, Point P3, Tab. 2.9, Point P1) were typical of the type of steel used in MC and MCP experimental series and showed correspondence to mol. % 94.0 Fe, 2.6 Cr, 1.5 Ni, 0.5 Mn, 0.9 Si, 0.4 Mo, 0.1 V. In proximity to the boundary, steel becomes depleted in admixtures (Tab. 2.7, P7; Tab. 2.10, P4) and the composition corresponds to (mol. %) 96.1 Fe, 1.0 Cr, 2.1 Ni, 0.4 Si, 0.4 Mo. At the same time, an increase in Ni concentration is observed.

Let's consider structure of the zone of interaction with steel in the direction from the periphery to the central part. A monophase ~250 µm-thick layer (Fig. 2.6, Region 1-1) is visible

in the polished section periphery. The very boundary with steel contains orbicular inclusions of a spinel-based phase $\text{Fe}[\text{CrFe}]\text{O}_4$ with an increased (relative to steel) content of Si and Mn (Fig. 2.6, Regions 1-1-1-3 and 1-1-4, Tab. 2.7, Points P9 and P14). The presence of oxidic inclusions in metal and their shape witness their liquid-phase origin. Then, there follows a $\sim 50\text{-}100\ \mu\text{m}$ -thick layer composed predominantly of the FeO-based phase (Fig. 2.6, Regions 1-1-1-1, 1-1-1-2 and 1-1-1-3, Tab. 2.7, Squares SQ1 and SQ8, Points P4 and P8). Besides the mentioned phase, at least two more phases can be identified in the layer in question: one with high uranium content (Points P1 and P5) and a $\gamma\text{-(Fe,Ni)}$ solid solution-based one (Points P2 and P6). It should be noted that the uranium-bearing phase was observed right up to the layer that contains orbicular spinel inclusions. Also, it is important to pay attention at the eutectically crystallized inclusions in this layer, more precisely, inclusions of the $\gamma\text{-(Fe,Ni)}$ solid solution (Region 1-1-4, Tab. 2.7, Squares SQ6 and SQ7). The rounded shape of phases and the presence of zones with eutectic character of crystallization indicate the liquid-phase nature of this layer formation. The considered layer is followed by another, approximately $200\ \mu\text{m}$ -thick one, with large rounded pores. This layer is composed of the same phases as the previous one, but there is more of eutectics and $\gamma\text{-(Fe,Ni)}$ and less of the FeO-based phase in it (Regions 1-1-1-4 and 1-1-3, Squares SQ2 and SQ5). Above this layer there is another one, rich in the refractory oxidic component (Region 1-1-2, Point P10). The presence of eutectically crystallized regions in the FeO-based phase (Region 1-1-2, SQ4) should be noted. This oxidic eutectics has a different U/Zr ratio in comparison with the metallic eutectics which had been registered in the underlying layer (compare, e.g. SQ4 and SQ6).

Therefore, the presence of liquid phase can be ascertained for the entire zone in question.

When moving from the periphery to the center, the obvious changes are as follows. The layer that consists predominantly of the FeO-based phase disappears. The amounts of metallic eutectics and $\gamma\text{-(Fe,Ni)}$ solid solution increases, and $50\text{-}100\ \mu\text{m}$ -sized orbicular inclusions on the basis of the $\gamma\text{-(Fe,Ni)}$ solid solution start appearing in the upper part of the zone (Fig. 2.7, Tab. 2.8, Point P3; Fig. 2.8, Tab. 2.9, Point P2). A more fine-dispersed character and alignment of the spinel-based phase along the steel grain boundaries have also been recorded (Fig. 2.7, Regions 2-1 and 2-1-1).

Closer to the central part there were observed dendritic branched cracks, which are characteristic of the stress corrosion cracking regime (Fig. 2.8, Region 6; Fig. 2.9, Regions 7-2 and 9). In addition, the layer containing much FeO and metallic eutectics disappears in the central part. Instead, the steel is directly joined by the layer of a phase based on the $\gamma\text{-(Fe,Ni)}$ solid solution (Fig. 2.9, Region 8-1, Fig. 2.10, Region 10-13). This layer was found to contain an insignificant number of droplet-shaped inclusions of the FeO-based phase.

The analysis of the oxidic part of the ingot yielded a conclusion about high amounts of iron in it (Figs. 2.11-2.13, Tabs. 2.11-2.13 all SQ; Fig. 2.15, Tab. 2.14, SQ2). Starting with Region 16, a layer may be identified that would be insignificantly richer in the refractory component in comparison with the crystallized melt bulk. Also, this layer manifests iron-rich orbicular inclusions (Fig. 2.11, Region 5-1; Fig. 2.13, Region 18, Tab. 2.13, SQ2; Fig. 2.14, Region 19-1). Their presence confirms that there used to be a liquid phase in this layer. A more detailed microstructural investigation in the near-boundary area has discovered the eutectically crystallized regions (Fig. 2.11, Regions 15-1-1-1, 15-1-1-1-1 and 15-1-1-1-1-1, Tab. 2.11, SQ4 and P3). This is another confirmation of the liquid phase presence in this layer.

Therefore, it may be concluded that the corrosion layer on that part of the steel surface where it could be registered was predominantly or completely composed of a liquid phase. Besides, the liquid phase was present in the corium crust adjacent to the steel surface (to the corrosion layer).

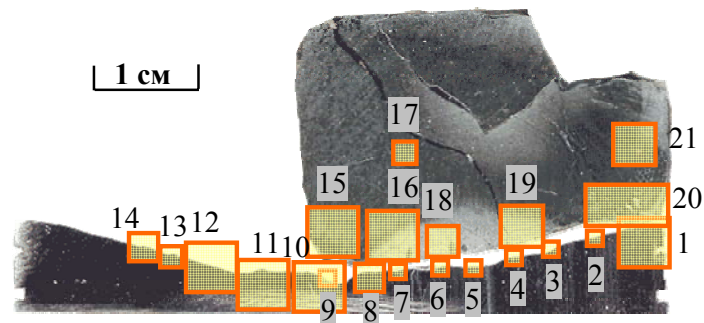


Fig. 2.5 – Polished section from MCP-2 with regions marked for SEM/EDX examination

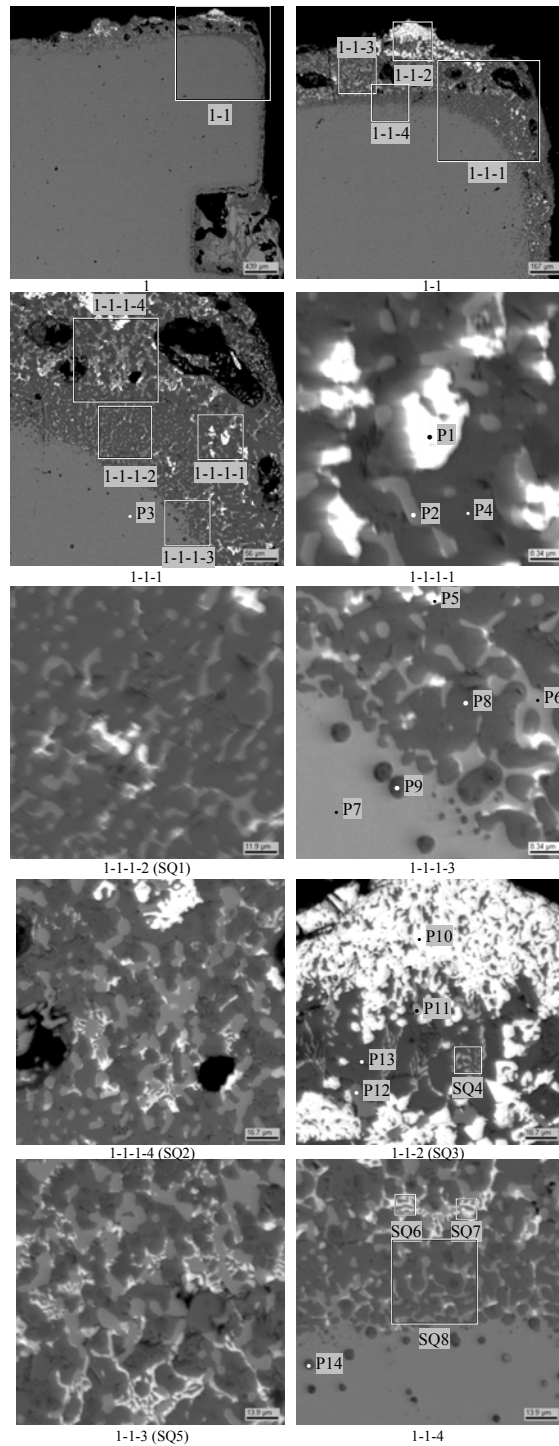


Fig. 2.6 – Micrographs of region 1

Table 2.7

EDX data for region 1												
No.		U	Zr	Fe	Cr	Ni	Si	Mn	Mo	V	~O	Phase
SQ1	mass %	2.46	2.17	71.82	3.67	2.36	0.27	0.25	0.79		16.21	-
	mol. %	0.42	0.96	52.14	2.86	1.63	0.39	0.19	0.33	-	41.07	
	mol. % MeO _x	0.71	1.64	88.49	4.85	2.77	0.66	0.32	0.57			
SQ2	mass %	6.44	3.22	60.68	6.98	4.35	0.35	0.28	0.90		16.81	-
	mol. %	1.11	1.45	44.63	5.52	3.04	0.50	0.21	0.39	-	43.16	
	mol. % MeO _x	1.95	2.55	78.51	9.71	5.35	0.89	0.36	0.68			
SQ3	mass %	41.52	4.19	32.07	2.49	1.61	0.29	0.17	0.27		17.40	-
	mol. %	8.84	2.33	29.10	2.42	1.39	0.52	0.16	0.14	-	55.10	
	mol. % MeO _x	19.69	5.18	64.82	5.40	3.10	1.15	0.35	0.31			
SQ4	mass %	12.83	14.91	58.91	1.14			0.22			12.00	Eutectics
	mol. %	2.63	7.98	51.50	1.07	-		0.20	-		36.62	
	mol. % MeO _x	4.15	12.59	81.27	1.68			0.31				
SQ5	mass %	7.90	5.07	63.83	8.49	4.60	0.36	0.32	0.86		8.58	-
	mol. %	1.63	2.73	56.11	8.02	3.85	0.63	0.28	0.44	-	26.32	
	mol. % MeO _x	2.21	3.70	76.15	10.88	5.22	0.86	0.38	0.59			
SQ6	mass %	33.47	5.23	55.34	2.12	3.38			0.46			Eutectics
	mol. %	10.89	4.44	76.70	3.15	4.46	-		0.37	-		
SQ7	mass %	35.94	7.00	50.42	2.31	1.08	0.17				3.08	Eutectics
	mol. %	10.85	5.51	64.85	3.19	1.32	0.43			-	13.85	
	mol. % MeO _x	12.59	6.40	75.28	3.70	1.54	0.50					
SQ8	mass %	2.28	2.09	76.56	3.91	2.34	0.19	0.39	0.52	0.19	11.54	-
	mol. %	0.42	1.01	60.59	3.32	1.76	0.30	0.31	0.24	0.16	31.88	
	mol. % MeO _x	0.62	1.48	88.94	4.88	2.58	0.44	0.46	0.35	0.24		
P1	mass %	83.17	2.56	4.59			0.17				9.51	(U,Zr)O ₂
	mol. %	32.96	2.65	7.75	-		0.58			-	56.06	
	mol. % MeO _x	75.02	6.02	17.64			1.33					
P2	mass %			83.20	1.10	12.69	0.21		1.72		1.07	γ-(Fe,Ni)
	mol. %	-		81.87	1.16	11.88	0.42	-	0.99	-	3.68	
	mol. % MeO _x			85.00	1.21	12.33	0.43		1.02			
P3	mass %			94.20	2.48	1.54	0.47	0.52	0.78			Steel
	mol. %	-		93.96	2.65	1.46	0.93	0.53	0.46	-		
P4	mass %	0.22	0.76	70.24	4.76		0.18	0.23			23.61	FeO
	mol. %	0.03	0.29	44.21	3.22	-	0.22	0.15		-	51.88	
	mol. % MeO _x	0.07	0.61	91.86	6.69		0.47	0.31				
P5	mass %	85.06	2.85	10.54	0.41	0.51					0.63	U(Zr) ₂ Fe
	mol. %	56.43	4.93	29.82	1.26	1.36				-	6.21	
	mol. % MeO _x	60.17	5.26	31.79	1.34	1.45						
P6	mass %			87.65	0.64	8.80	0.15		2.76			γ-(Fe,Ni)
	mol. %	-		88.88	0.70	8.49	0.30	-	1.63	-		
P7	mass %			96.05	1.51	1.42	0.23		0.78			Steel
	mol. %	-		96.11	1.62	1.35	0.46		0.46	-		
P8	mass %		0.85	71.51	5.22		0.29	0.47	0.61	0.20	20.86	FeO
	mol. %	-	0.34	47.02	3.69	-	0.38	0.31	0.23	0.14	47.89	
	mol. % MeO _x		0.66	90.23	7.07		0.72	0.60	0.45	0.27		
P9	mass %			38.60	19.49	0.28	1.83	3.57		0.90	35.34	Fe[CrFe]O ₄
	mol. %	-		20.17	10.93	0.14	1.90	1.90		0.51	64.45	
	mol. % MeO _x			56.74	30.76	0.39	5.34	5.33		1.45		

P10	mass %	88.08	2.31	0.48	0.06					9.07	U(Zr)O ₂		
	mol. %	38.07	2.61	0.89	0.12	-				58.31			
	mol. % MeO _x	91.32	6.25	2.14	0.30								
P11	mass %	29.73	36.65	11.69			0.43			21.51	Zr(U)O ₂		
	mol. %	5.96	19.17	9.98	-		0.73	-		64.15			
	mol. % MeO _x	16.63	53.48	27.85			2.04						
P12	mass %	-		74.31	-	24.22	-		1.46	-		γ-(Fe,Ni)	
	mol. %			75.66		23.47			0.87				
P13	mass %	-		0.37	76.26	0.99	0.29	0.17	0.35	0.42	21.16	FeO	
	mol. %			0.15	49.97	0.70	0.18	0.22	0.23	0.16	48.40		
	mol. % MeO _x			0.28	96.83	1.35	0.35	0.43	0.45	0.31			
P14	mass %	-		31.95	18.70	-		4.18	5.16	0.29	1.17	38.54	Fe[CrFe]O ₄
	mol. %			15.85	9.96			4.12	2.60	0.08	0.64	66.74	
	mol. % MeO _x			47.66	29.95			12.40	7.82	0.25	1.92		

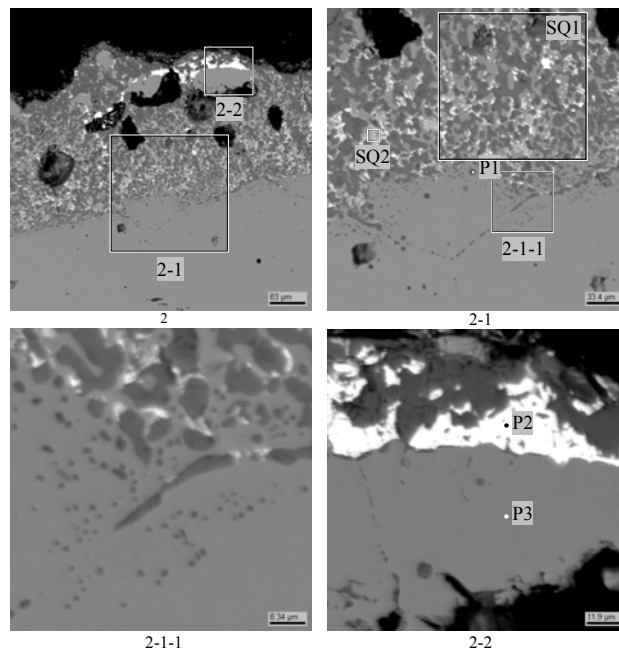


Fig. 2.7 – Micrographs of region 2

Table 2.8

EDX data for region 2												
No.		U	Zr	Fe	Cr	Ni	Si	Mn	Mo	V	~O	Phase
SQ1	mass %	6.01	3.58	58.21	5.27	3.34	0.47		0.78		22.34	-
	mol. %	0.94	1.46	38.80	3.77	2.12	0.62	-	0.30	-	51.99	
	mol. % MeO _x	1.96	3.04	80.81	7.85	4.41	1.29		0.63			
SQ2	mass %	28.70	6.85	58.23	2.47	2.82	0.16		0.53		0.23	Eutectics
	mol. %	8.87	5.52	76.68	3.50	3.54	0.43	-	0.40	-	1.06	
	mol. % MeO _x	8.96	5.58	77.50	3.53	3.58	0.43		0.41			
P1	mass %	-		58.91	13.48	0.50	3.48	3.26	0.51	0.59	19.28	Fe[CrFe]O ₄
	mol. %			38.68	9.50	0.31	4.54	2.17	0.20	0.42	44.18	
	mol. % MeO _x			69.28	17.02	0.56	8.14	3.89	0.35	0.75		
P2	mass %	94.86	3.54	1.61	-							U(Zr,Fe)(O)
	mol. %	85.51	8.32	6.18								
P3	mass %	-		70.34	-	28.28	-		1.38	-		γ-(Fe,Ni)
	mol. %			71.74		27.44			0.82			

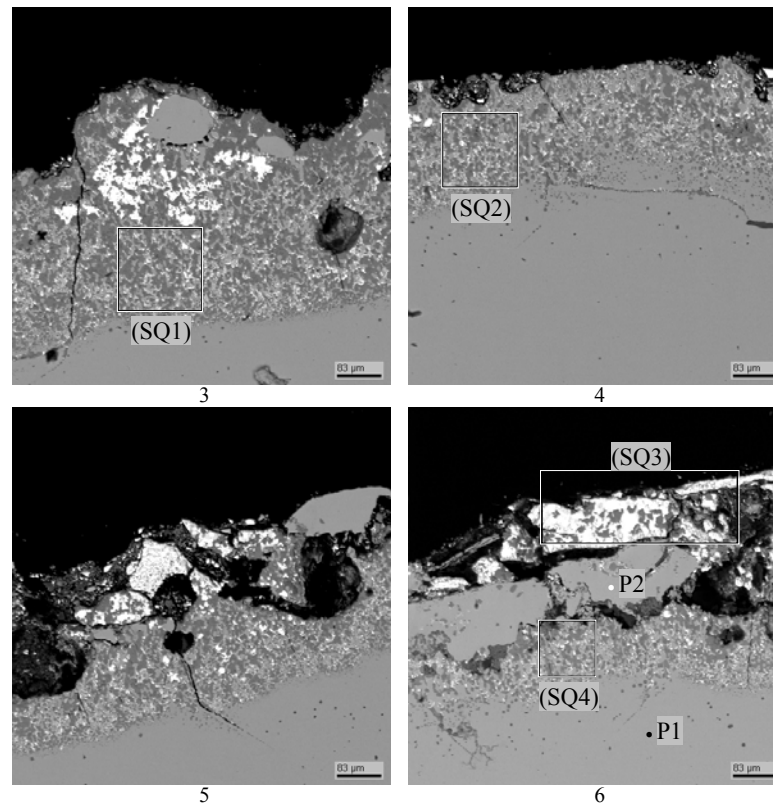


Fig. 2.8 – Micrographs of regions 3-6

Table 2.9

		EDX data for regions 3-6										
No.		U	Zr	Fe	Cr	Ni	Si	Mn	Mo	V	~O	Phase
SQ1	mass %	7.34	3.66	43.27	5.32	3.10	0.23		0.40	0.14	36.54	-
	mol. %	0.93	1.22	23.48	3.10	1.60	0.25	-	0.12	0.08	69.21	
	mol. % MeO _x	3.03	3.95	76.25	10.08	5.20	0.81		0.41	0.26		
SQ2	mass %	6.53	5.12	66.54	2.98	2.26	0.52	0.33	0.81		14.93	-
	mol. %	1.17	2.40	50.99	2.45	1.65	0.79	0.26	0.36	-	39.93	
	mol. % MeO _x	1.95	4.00	84.89	4.08	2.74	1.31	0.42	0.60			
SQ3	mass %	15.53	5.29	9.41	3.54	0.73	0.38				65.11	-
	mol. %	1.46	1.30	3.78	1.53	0.28	0.31		-		91.34	
	mol. % MeO _x	16.91	15.03	43.65	17.63	3.23	3.55					
SQ4	mass %	7.36	4.83	64.74	4.06	3.90	5.72		0.76		8.61	-
	mol. %	1.45	2.48	54.23	3.66	3.11	9.53	-	0.37	-	25.18	
	mol. % MeO _x	1.93	3.31	72.47	4.89	4.16	12.74		0.50			
P1	mass %			94.32	2.41	1.53	0.44	0.42	0.71	0.17		Steel
	mol. %			94.07	2.58	1.45	0.87	0.42	0.41	0.19	-	
P2	mass %			78.50	0.30	19.69			1.51			γ-(Fe,Ni)
	mol. %			79.75	0.33	19.03			0.89		-	

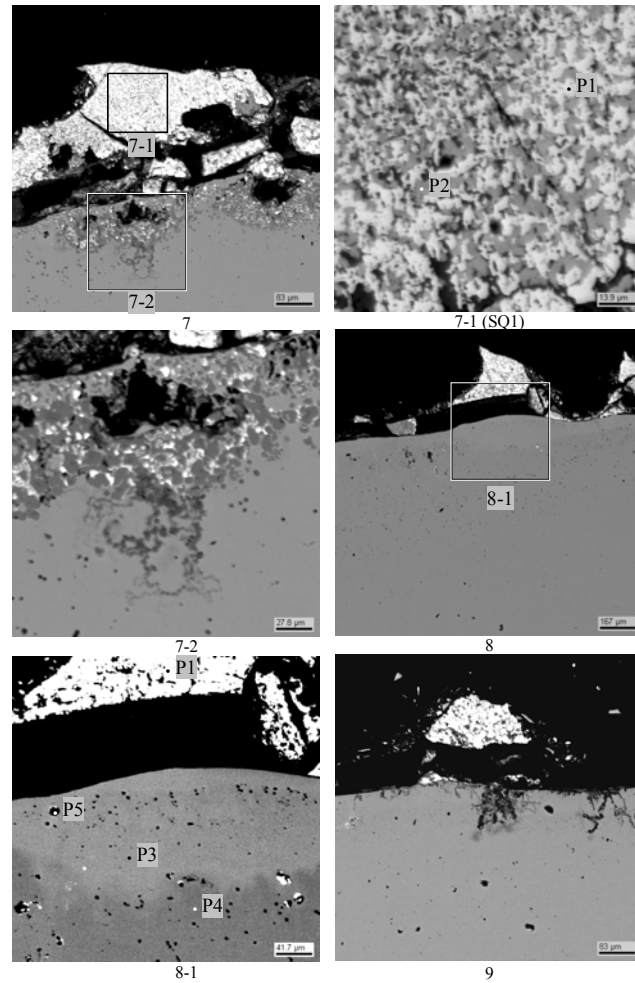


Fig. 2.9 – Micrographs of regions 7-9

Table 2.10

EDX data for regions 7-9												
No.		U	Zr	Fe	Cr	Ni	Si	Mn	Mo	V	~O	Phase
SQ1	mass %	53.03	15.05	14.92	0.30	-	0.19	0.22	-	-	16.31	-
	mol. %	13.18	9.76	15.80	0.34		0.39	0.24			60.30	
	mol. % MeO _x	33.19	24.57	39.81	0.84		0.99	0.61				
P1	mass %	83.42	6.39	2.62							7.57	(U,Zr)O ₂
	mol. %	37.26	7.44	4.99							50.31	
	mol. % MeO _x	74.98	14.98	10.04								
P2	mass %	39.64	38.26	9.34							12.76	(Zr,U)O ₂
	mol. %	10.74	27.05	10.78							51.43	
	mol. % MeO _x	22.11	55.69	22.20								
P3	mass %	-		68.43	-	30.19	-		1.38	-		γ-(Fe,Ni)
	mol. %	-		69.85	-	29.33	-		0.82	-		
P4	mass %	-		95.76	0.36	3.08	0.16	-	0.64	-		Steel
	mol. %	-		95.99	0.39	2.94	0.32	-	0.37	-		
P5	mass %	0.21	0.40	73.92	0.65	0.72	0.30	-	0.51	-	23.30	FeO
	mol. %	0.03	0.16	46.84	0.44	0.43	0.38	-	0.19	-	51.53	
	mol. % MeO _x	0.07	0.32	96.64	0.91	0.89	0.79	-	0.39	-		

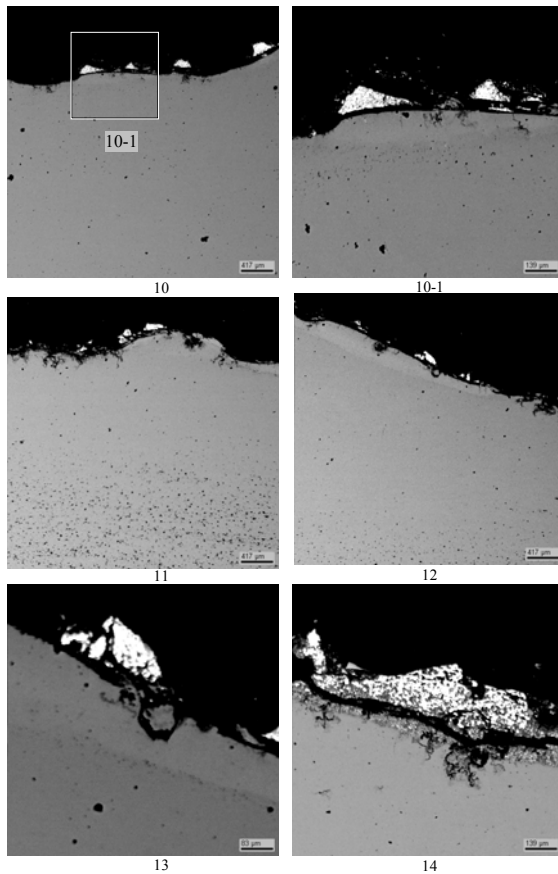


Fig. 2.10 – Micrographs of regions 10-14

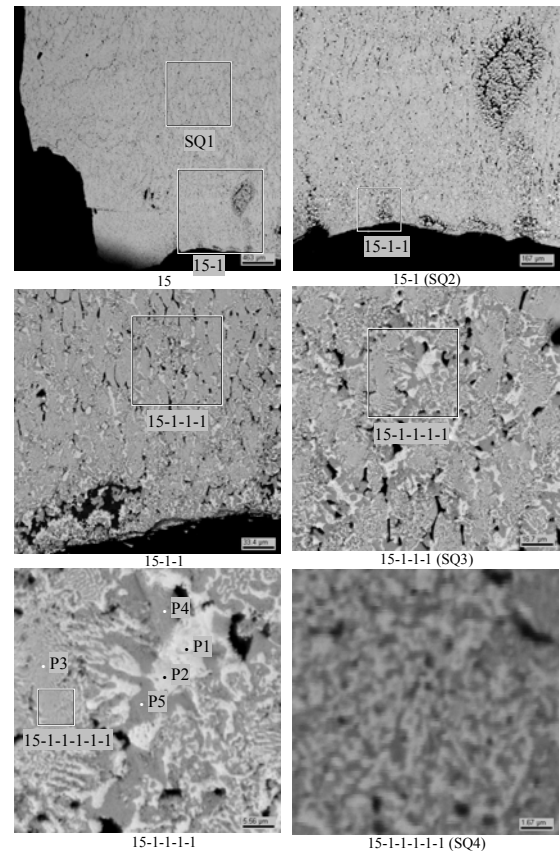


Fig. 2.11 – Micrographs of region 15

Table 2.11

EDX data for region 15												
No.		U	Zr	Fe	Cr	Ni	Si	Mn	Mo	V	~O	Phase
SQ1	mass %	58.84	19.49	5.00							16.67	-
	mol. %	15.52	13.41	5.62							65.44	
	mol. % MeO _x	44.91	38.81	16.28								
SQ2	mass %	58.80	20.08	5.43							15.68	-
	mol. %	15.99	14.25	6.30							63.45	
	mol. % MeO _x	43.76	39.00	17.23								
SQ3	mass %	60.46	20.96	6.40			0.14				12.04	-
	mol. %	18.73	16.94	8.46	-		0.37				55.50	
	mol. % MeO _x	42.10	38.07	19.00			0.83					
SQ4	mass %	61.38	21.3	4.12			0.16				13.04	Eutectics
	mol. %	18.61	16.85	5.32	-		0.40				58.82	
	mol. % MeO _x	45.20	40.92	12.93			0.95					
P1	mass %	82.62	8.87	1.97							6.54	(U,Zr(Fe))(O)
	mol. %	39.06	10.94	3.97							46.02	
	mol. % MeO _x	72.37	20.27	7.36								
P2	mass %	82.24	8.09	1.41							8.26	(U,Zr(Fe))(O)
	mol. %	35.41	9.09	2.59							52.9	
	mol. % MeO _x	75.17	19.31	5.52								
P3	mass %	59.54	19.58	3.63							17.24	Eutectics (compare with SQ4)
	mol. %	15.56	13.35	4.05							67.04	
	mol. % MeO _x	47.21	40.51	12.28								
P4	mass %	45.93	29.76	5.20							19.11	(Zr,U(Fe))O ₂
	mol. %	10.68	18.06	5.16							66.10	
	mol. % MeO _x	31.51	53.27	15.22								
P5	mass %	47.92	30.18	4.36			0.20				17.34	(Zr,U(Fe))O ₂
	mol. %	11.83	19.45	4.59	-		0.42				63.71	
	mol. % MeO _x	32.61	53.60	12.63			1.16					

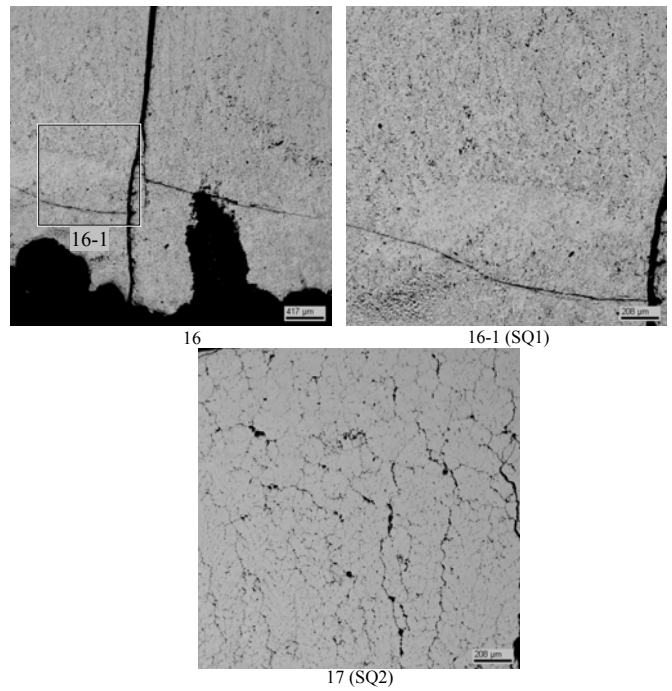


Fig. 2.12 – Micrographs of regions 16 and 17

Table 2.12

		EDX data for regions 16 and 17										
No.		U	Zr	Fe	Cr	Ni	Si	Mn	Mo	V	~O	Phase
SQ1	mass %	60.82	20.28	6.02			0.15				12.73	-
	mol. %	18.43	16.04	7.77	-		0.39		-		57.37	
	mol. % MeO _x	43.23	37.62	18.23			0.92					
SQ2	mass %	60.36	19.88	4.76							14.99	-
	mol. %	16.97	14.59	5.71			-				62.73	
	mol. % MeO _x	45.54	39.14	15.32								

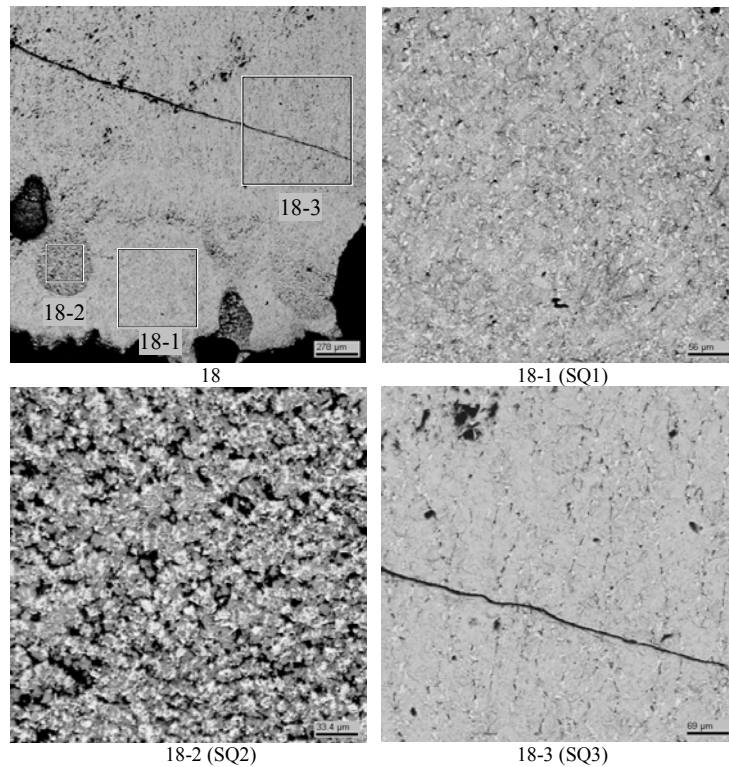


Fig. 2.13 – Micrographs of region 18

Table 2.13

EDX data for region 18												
No.		U	Zr	Fe	Cr	Ni	Si	Mn	Mo	V	~O	Phase
SQ1	mass %	53.36	18.32	4.68							23.64	-
	mol. %	11.29	10.11	4.22							74.39	
	mol. % MeO _x	44.06	39.46	16.47								
SQ2	mass %	48.48	18.98	15.78	0.42		0.24				16.11	-
	mol. %	11.86	12.11	16.45	0.47	-	0.49		-		58.62	
	mol. % MeO _x	28.66	29.27	39.75	1.15		1.18					
SQ3	mass %	52.23	17.64	4.30				0.13			25.71	-
	mol. %	10.44	9.20	3.66				0.22		-	76.48	
	mol. % MeO _x	44.39	39.12	15.57				0.92				

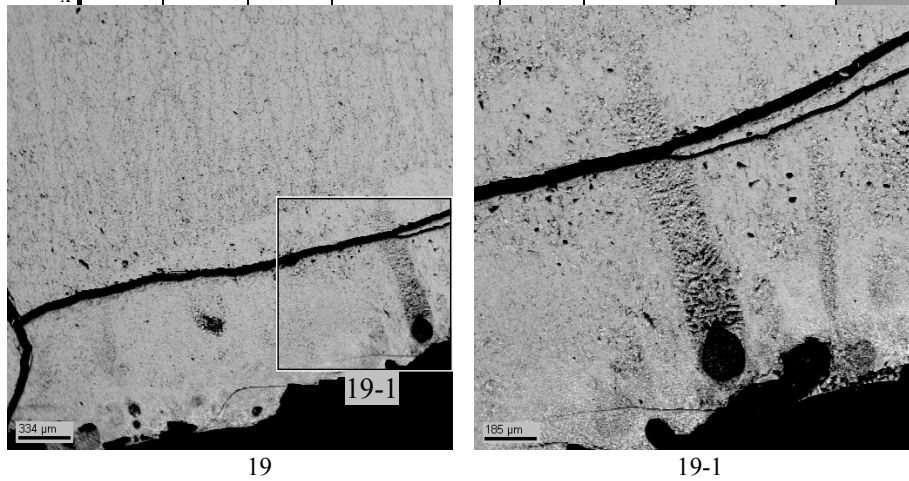


Fig. 2.14 – Micrographs of region

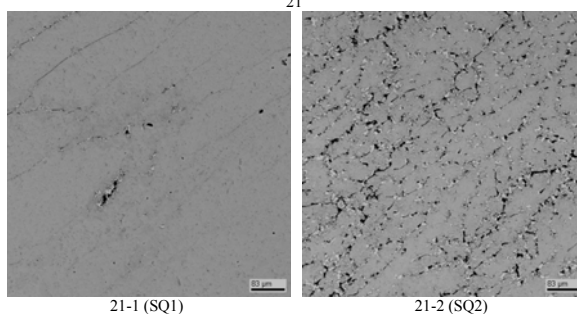
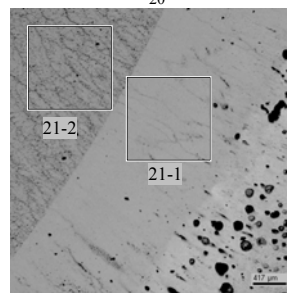
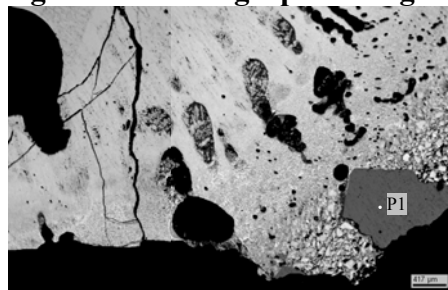


Fig. 2.15 – Micrographs of regions 20 and 21

Table 2.14

		EDX data for region 20 and 21										
No.		U	Zr	Fe	Cr	Ni	Si	Mn	Mo	V	~O	Phase
SQ1	mass %	62.17	20.35	2.23							15.25	(U,Zr)O ₂
	mol. %	17.68	15.10	2.70							64.53	
	mol. % MeO _x	49.83	42.55	7.62								
SQ2	mass %	57.99	19.83	5.7	0.37		0.14				15.97	-
	mol. %	15.49	13.82	6.48	0.45	-	0.32				63.43	
	mol. % MeO _x	42.35	37.78	17.74	1.24		0.89					
P1	mass %		71.26			0.35					28.39	ZrO ₂
	mol. %	-	30.50	-		0.23					69.27	
	mol. % MeO _x		99.24			0.76						

3. DISCUSSION OF RESULTS

3.1 Preliminary generalization of experimental data

The results of experimental investigations of the interaction of molten UO_{2+x}-ZrO₂-FeO_y corium with vessel steel [2] allowed offering a model of corrosion and obtaining a semiempirical correlation generalizing experimental data. The model was based on a supposition that the rate of corrosion is determined by the Fe ions diffusion through the corrosion layer Fe_{1-x}O, which forms at the steel surface, and on an assumption of constancy of this layer thickness when temperature of the interaction interface changes. The initial correlation was written as follows:

$$\frac{W}{q} = A_1 \exp\left(-\frac{E_{a1}}{RT_S}\right), \quad (1)$$

where W is the corrosion rate, m/s;

q is the heat flux, MW/m²;

A is the preexponential factor;

E_a is the activation energy, J/mol.;

$R=8.314$ J/(mol. K) is the universal gas constant;

T_S is the interface surface temperature, K.

However, experimental data generalization on semilogarithmic coordinates

$\frac{W}{q} = f\left(\frac{1000}{T_S}\right)$ (see Fig. 3.1) has shown that at $T_S > 1050^\circ\text{C}$ the function slope increases, which

signifies, within the accepted coordinates, an increase of E_a , i.e. intensification of corrosion. The SEM/EDX results helped to explain the mentioned effect in such a way that a liquid phase forms in the corrosion layer and reduces its diffusion resistance. Therefore, the correlation has been finally written as:

$$\frac{W}{q} = A_1 \exp\left(-\frac{E_{a,1}}{RT_S}\right) + A_2 \exp\left(-\frac{E_{a,2}}{RT_S}\right). \quad (2)$$

$$\frac{W}{q}, \frac{\text{m}}{\text{s}}, \frac{\text{m}^2}{\text{MW}}$$

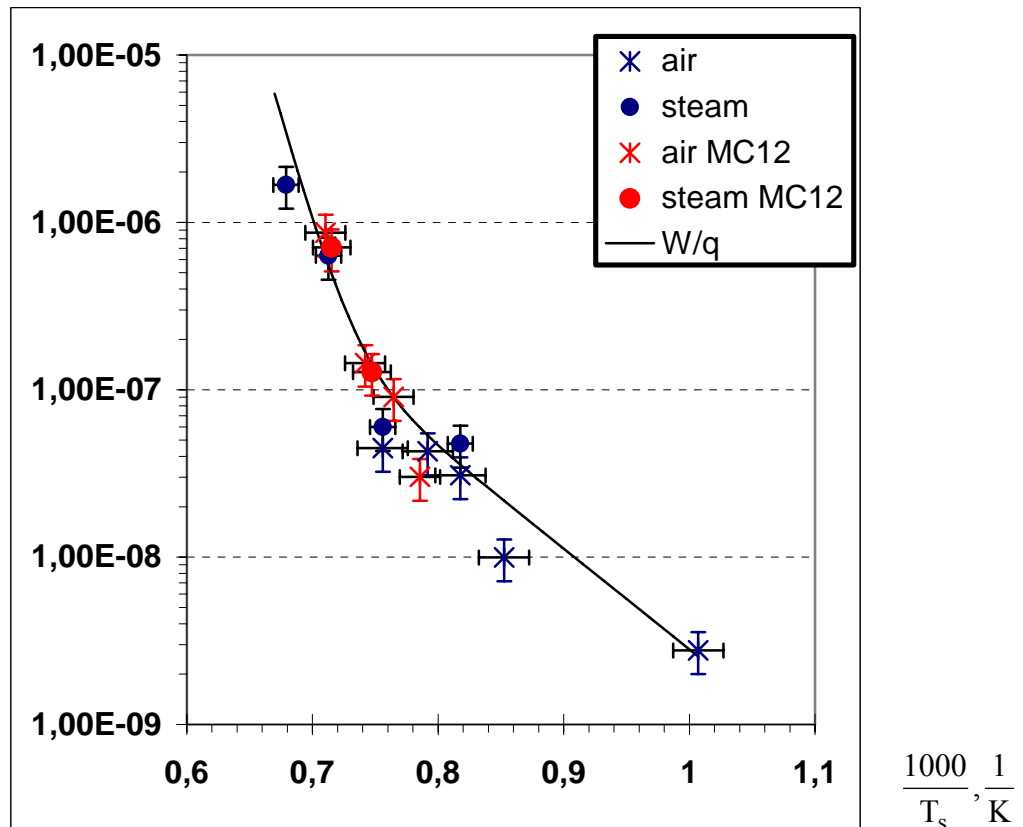


Fig. 3.1 – Generalization of experimental data on kinetics of corrosion of steel at its interaction with molten $\text{UO}_{2+x}\text{-ZrO}_2\text{-FeO}_y$ in the oxidizing atmosphere [2]

In Fig. 3.2, experimental data from MC10 and MCP-2 involving molten $\text{UO}_{2+x}\text{-ZrO}_2$, are given in the same coordinates as in Fig. 3.1. First of all it should be mentioned that the composition of atmosphere (steam, air) had practically no effect on the rate of corrosion, like in the case with molten $\text{UO}_{2+x}\text{-ZrO}_2\text{-FeO}_y$. However, a significant difference from the results presented in Fig. 3.1 is obvious – i.e. there is no intensification of corrosion, that is, the dependence that generalizes experimental data is written as (1) instead of (2). The absence of corrosion intensification in the high-temperature domain, as it follows from Fig. 3.2, does not agree with the results of SEM/EDX analysis, which evidence that at the maximum interface surface temperature (T_s) of 1370°C, achieved in MCP-2, practically the entire corrosion layer was liquid-phase.

Obviously, the obtained results cannot be explained by the process model offered in [2] and require development of new concepts concerning the model.

$$\frac{W}{q} \cdot \frac{\text{m}}{\text{s}} \frac{\text{m}^2}{\text{MW}}$$

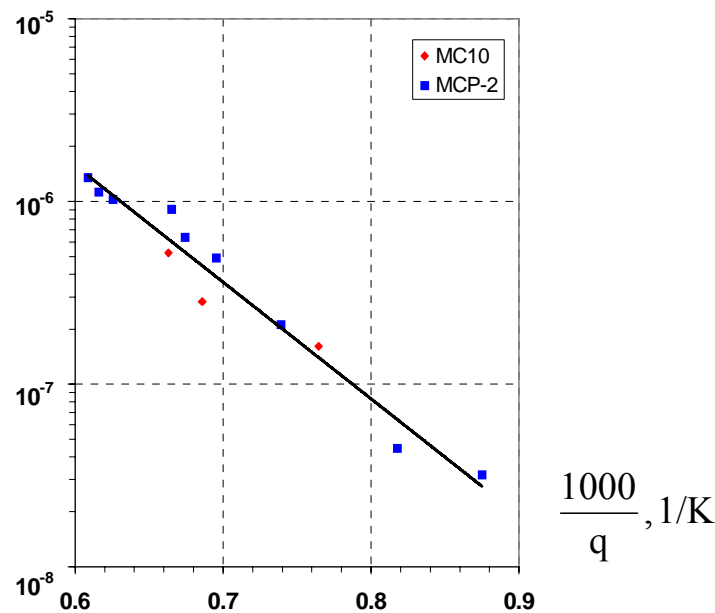


Fig. 3.2 – Preliminary generalization of the results of tests with the $\text{UO}_{2+x}\text{-ZrO}_2$. corium

3.2 Corrosion model

When analyzing the results of METCOR tests with the oxidized corium until recently, Fe^{2+} diffusion in the Fe_{1-x}O layer has been regarded as the basic process determining the rate of corrosion. In accordance with the Tamman's equation [9], the rate of corrosion is expressed as:

$$W = \frac{dh}{dt} = A \exp\left(-\frac{E_a}{RT}\right) \frac{1}{\delta}, \text{ m/s}; \quad (3)$$

where h is the depth of corrosion, m;
 δ is the thickness of the Fe_{1-x}O layer, m.

The value of δ is proportionate to the depth of corrosion h during steel corrosion in air (without corium), hence a correlation has been obtained in [10], which generalizes relevant experimental data [11] for the 15Kh2NMFA-A steel:

$$W = \frac{1}{2} \left[3.32 \cdot 10^{-7} \exp\left(-\frac{1.2 \cdot 10^5}{RT}\right) \right]^{1/2} t^{-1/2}, \text{ m/s}, \quad (4)$$

where t is the time, s.

The value of activation energy (E_a) of $1.2 \cdot 10^5$ J/mol. corresponds to the value obtained using experimental data from [12, 13] for Fe^{2+} diffusion in Fe_{1-x}O , i.e., $E_a = (1.0 \dots 1.5) \cdot 10^5$ J/mol.

Generalization of experimental data on the interaction of molten $\text{UO}_{2+x}\text{-ZrO}_2\text{-FeO}_y$ corium with steel in nitrogen has yielded similar results [10, 11]. The SEM/EDX analysis has shown a dense Fe_{1-x}O layer to exist in this test on the steel surface at the interface surface temperature (T_s) of 1200°C. The correlation generalizing experimental data is written in [10] as

$$W = \frac{1}{2} \left[3.4 \cdot 10^{-7} \exp\left(-\frac{1.26 \cdot 10^5}{RT}\right) \right]^{1/2} t^{-1/2}, \text{ m/s}, \quad (5)$$

i.e., is close to (4). Similarity of these correlations indicates that the process of steel corrosion does not differ from that in air under oxygen deficiency in molten corium.

Now, the results of tests on the interaction of steel with molten coriums in the oxidizing atmosphere should be considered. The first qualitative difference from corrosion in an inert above-melt atmosphere and in air without corium (already noticed in [11]) is that the rate of corrosion is independent from time. The model of the process offered in [2] explained this difference by supposing that the Fe_{1-x}O layer thickness stabilizes (i.e., does not grow with time) as a result of O^{2-} diffusion through the corium crust to the corrosion layer and the oppositely directed Fe^{2+} diffusion from the corrosion layer surface into the melt through the corium crust in the oxidizing above-melt atmosphere. However, the time independence of corrosion rate may be interpreted in a wider sense, in particular as a consequence of constancy over time of diffusion resistance against the Fe^{2+} mass flow from the interaction interface (from steel surface) to molten corium.

What may be regarded as diffusion resistance under the considered conditions? Let's take into consideration the above-mentioned (see Section 3.1) circumstance, that is, maintenance of constant value of the activation energy over a wide range of the interface temperature variation, which is confirmed by the results of MC10 and MCP-2 presented in Fig.3.2. At the same time, according to the SEM/EDX results, the corrosion layer was liquid at $T_S \approx 1370^\circ\text{C}$, while there are absolutely no reasons to expect appearance of a liquid phase in it at low temperatures ($870 \dots 950^\circ\text{C}$). Therefore, under the considered conditions the corrosion layer cannot be regarded as the diffusion resistance (at least, the decisive one) to the Fe^{2+} flow. In this case, the only obvious diffusion resistance is the corium crust. At low interface temperatures, when the solid Fe_{1-x}O layer undoubtedly exists, its thickness is much smaller than that of corium crust. This is confirmed by the results of the MC2 posttest analyses [11]. Therefore, diffusion resistance of the corrosion layer may be neglected, at least in this area of parameters determining corrosion. It is even more negligibly small at the appearance of the liquid determined by low eutectic temperature of the oxidized steel and corium components. As for steel corrosion in the tests with steel and molten corium interaction in an inert atmosphere, diffusion resistance is indeed ensured by the corrosion layer, like in the case of corrosion in air (without corium). This is determined by insufficiency of oxygen for Fe^{2+} diffusion under the conditions of corium low oxygen potential, which completely (or predominantly) limits the Fe^{2+} travel by thickness range of the Fe_{1-x}O layer which grows with time. Intensification of corrosion established in the tests with the $\text{UO}_{2+x}\text{-ZrO}_2\text{-FeO}_y$ corium (with a relatively low solidus temperature) at $T_S > 1050^\circ\text{C}$, may have an explanation that under these conditions the quantity of liquid phase in the corium crust becomes sufficient for the formation of percolation clusters which launch a different corrosion mechanism. This supposition is confirmed by the results of SEM/EDX analysis from MC12 [2] when traces of the liquid phase were discovered in the form of solid channels in both the corrosion layer right from its boundary with steel, and in the crust up to the crystallized corium.

In contrast to the above, no solid "channels" capable of reducing diffusion resistance of the crust have been discovered by SEM/EDX in the crust of the $\text{UO}_{2+x}\text{-ZrO}_2$ corium (with a high liquidus temperature) in MCP-2, though traces of the liquid phase have been observed.

Based on the above considerations, the model of corrosion can be developed for the conditions when the main diffusion resistance is provided by the corium crust. As before, it is based on the Tamman's equation:

$$W = A \exp\left(-\frac{E_a}{RT}\right) \frac{1}{\delta}. \quad (6)$$

However, δ in (6) is thickness of the corium crust instead of the corrosion layer. Its value is found from the thermal conductivity equation:

$$\delta = \frac{\lambda(T_{\text{sol}} - T_S)}{q}, \text{ m}, \quad (7)$$

where λ is thermal conductivity of the crust, MW/(mK);

T_{sol} , T_S are the solidus temperature of the composition of the corium crust, and of the steel surface, respectively, K;

q is the heat flux, MW/m².

The acceptance of constancy of λ and substitution of (7) into (6) yields:

$$\frac{W(T_{sol} - T_S)}{q} = A' \exp\left(-\frac{E_a}{RT}\right). \quad (8)$$

It should be noted that this is exactly the form [10], in which scanty experimental data for the UO_{2+x} - ZrO_2 - FeO_y corium have been generalized for a narrow range of T_S variation from 720 up to 1050°C.

3.3 Experimental data generalization

Tab. 3.1 summarizes all the data obtained in the METCOR and METCOR-P tests on the interaction of steel with molten coriums in the oxidizing atmosphere.

Table 3.1

Experimental results

Test	Corium	Atmosphere	Regime No.	Specimen surface temperature, °C	Heat flux, MW/m ²	Corrosion rate, mm/h
MC1	UO_{2+x} - ZrO_2 - FeO_y	air	1	950	0.90	0.1
MC2			1	900	0.39	0.014
			2	990	0.44	0.068
			3	1050	0.47	0.076
			4	720	0.30	0.003
MC10	UO_{2+x} - ZrO_2^*	steam	1	1035	0.95	0.55
2			1185	1.05	1.07	
3			1235	1.1	2.07	
MC11	UO_{2+x} - ZrO_2 - FeO_y	steam	1	950	0.99	0.17
2			1050	1.16	0.25	
3			1130	1.23	2.8	
4			1200	1.29	7.8	
MC12	UO_{2+x} - ZrO_2 - FeO_y	air	1	1000	0.92	0.10
			2	1035	0.95	0.31
			3	1075	0.98	0.51
			4	1135	1.04	3.25
		steam	5	1065	1.00	0.46
			6	1125	1.09	2.78
MCP-2	UO_{2+x} - ZrO_2^*	air	1	870	0.74	0.085
			2	950	0.81	0.13
			3	1080	0.92	0.7
			4	1165	1.0	1.77
			5	1210	1.04	2.38
			6	1230	1.06	3.46
			7	1325	1.15	4.25
			8	1350	1.17	4.75
			9	1370	1.19	5.8

* – initial composition

When generalizing experimental data, a question arises as to which temperature should be taken as the decisive one in the subexponential expression. Earlier, in [2], when the process of Fe^{2+} diffusion was considered only within the limits of a thin corrosion layer, this temperature was quite reasonably accepted to be equal to T_S . According to the new model, however, the temperature is significantly increasing as Fe ions move through the corium crust.

Let's introduce a notion of the effective temperature T_{ef} , the value of which lies within the $T_S \dots T_{sol}$ range. The following condition can help determine it. The time required by Fe ions to pass through the corium crust is:

$$t_1 = \int_0^{\delta} \frac{dz}{W}. \quad (9)$$

Taking into account the linear dependence of T on z, expression (9) can be transformed into:

$$t_1 = \frac{\delta}{T_{\text{sol}} - T_S} \int_{T_S}^{T_{\text{sol}}} \frac{dT}{W}. \quad (10)$$

For a concrete array of values of $T_{\text{sol}}-T_S$ and q, expression (8) can be written as:

$$W = A \exp\left(-\frac{E_a}{RT}\right). \quad (11)$$

By substituting (11) into (10), we obtain:

$$t_1 = \frac{\delta}{T_{\text{sol}} - T_S} \int_{T_S}^{T_{\text{sol}}} \frac{dT}{A \exp\left(-\frac{E_a}{RT}\right)} = \frac{\delta}{A(T_{\text{sol}} - T_S)} \int_{T_S}^{T_{\text{sol}}} \frac{dT}{\exp\left(-\frac{E_a}{RT}\right)}. \quad (12)$$

The effective temperature T_{ef} should be understood as a temperature, at which the constant velocity determined by expression (11) at $T = T_{\text{ef}}$ ensures equality of the time required by Fe ions to pass through the corium crust to that determined by expression (12):

$$t_1 = \frac{\delta}{A \exp\left(-\frac{E_a}{RT_{\text{ef}}}\right)}. \quad (13)$$

Thus, at any value of $T_{\text{sol}}-T_S$ and q, the value of T_{ef} will be determined by equality:

$$\frac{T_{\text{sol}} - T_S}{\exp\left(-\frac{E_a}{RT_{\text{ef}}}\right)} = \int_{T_S}^{T_{\text{sol}}} \frac{dT}{\exp\left(-\frac{E_a}{RT}\right)}. \quad (14)$$

It should be reminded that in (11)-(14) T is expressed in K.

The value of T_{ef} can be presented as:

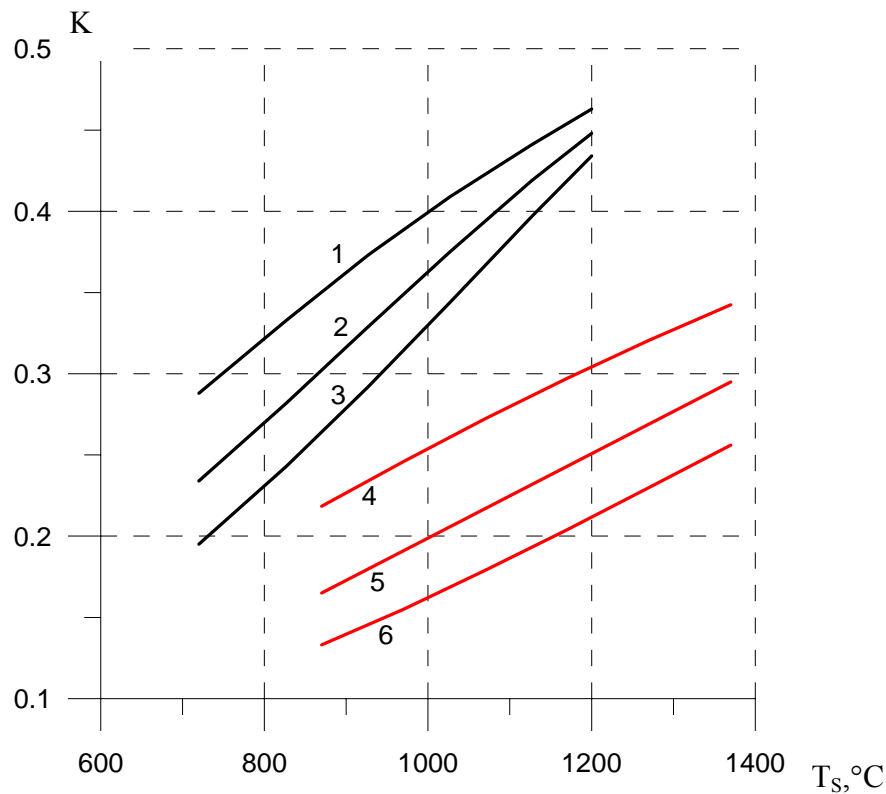
$$T_{\text{ef}} = T_S + K(T_{\text{sol}} - T_S) \quad (15)$$

and the integration of the right part of (14) yields the dependence of K on the determining parameters.

Fig. 3.3 offers the results of calculations made for two T_{sol} values, i.e., $T_{\text{sol}}=1340^\circ\text{C}$ ($\text{UO}_{2+x}\text{-ZrO}_2\text{-FeO}_y$ corium crust), $T_{\text{sol}}=2450^\circ\text{C}$ ($\text{UO}_{2+x}\text{-ZrO}_2$ corium crust) and three values of the activation energy $E_a=(1, 1.5, 2.0)\cdot 10^5$ J/mol. The value of K increases along with T_S grows and reduces with the decrease of T_{sol} and E_a . Therefore, an individual T_{ef} value that would differ from T_S should be taken for each point in the process of experimental data generalization.

In the first approximation, composition of the corium crust for which the indicated T_{sol} has been determined, may be regarded as close to that of the melt. The crust that forms under thermogradient conditions becomes enriched in the (U,Zr) O_{2+x} solid solution (refractory products of the melt primary crystallization), and it is compensated by the supply of iron oxides (the fusible component) from the corrosion layer.

For practical applications, it may be more rational to use T_S as the decisive temperature in generalizations. The results of experimental data generalization within the framework of the concepts described above are shown in Fig. 3.4. The error bars are set depending on the accuracy of W and q determination at 20 %, and at 30°C for T_S .



1, 2, 3 – $T_{\text{sol}}=1340^{\circ}\text{C}$; 4, 5, 6 – $T_{\text{sol}}=2450^{\circ}\text{C}$;
 1, 4 – $E_a=1\cdot 10^5 \text{ J/mol.}$; 2, 5 – $E_a=1.5\cdot 10^5$; 3, 6 – $E_a=2\cdot 10^5$

Fig. 3.3 – Dependence of K coefficient on the steel surface temperature in (15)

A correlation obtained for the $\text{UO}_{2+x}\text{-ZrO}_2$ corium is:

$$\frac{W(2723 - T_s)}{q} = 4.98 \exp\left(-\frac{1.1 \cdot 10^5}{RT_s}\right). \quad (16)$$

For the $\text{UO}_{2+x}\text{-ZrO}_2\text{-FeO}_y$ corium, the form of correlation is:

$$\frac{W(1613 - T_s)}{q} = 0.1 \exp\left(-\frac{0.91 \cdot 10^5}{RT_s}\right) + 3.4 \cdot 10^{14} \exp\left(-\frac{4.99 \cdot 10^5}{RT_s}\right). \quad (17)$$

It should be kept in mind that with such a treatment, the obtained values of activation energy differ from true values which characterize diffusion of Fe ions in corium crust.

Fig. 3.5 offers experimental data processed using T_{ef} .

After such a processing, the correlations generalizing experimental data take the following form:

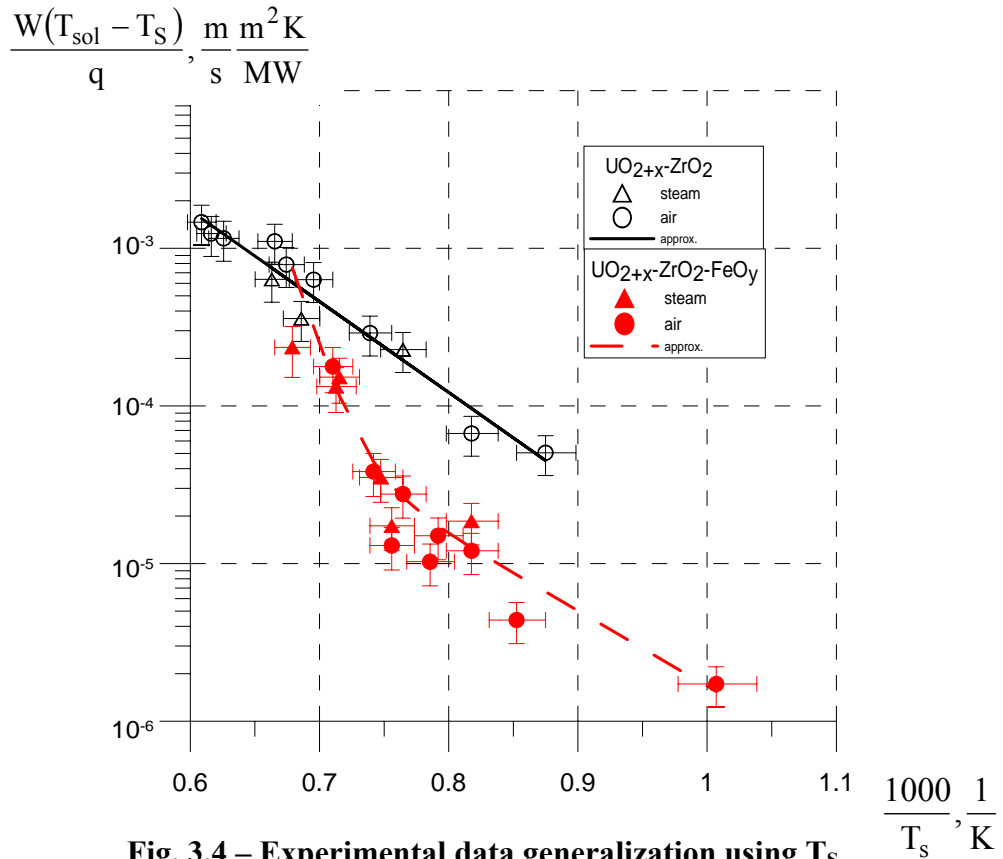


Fig. 3.4 – Experimental data generalization using T_S

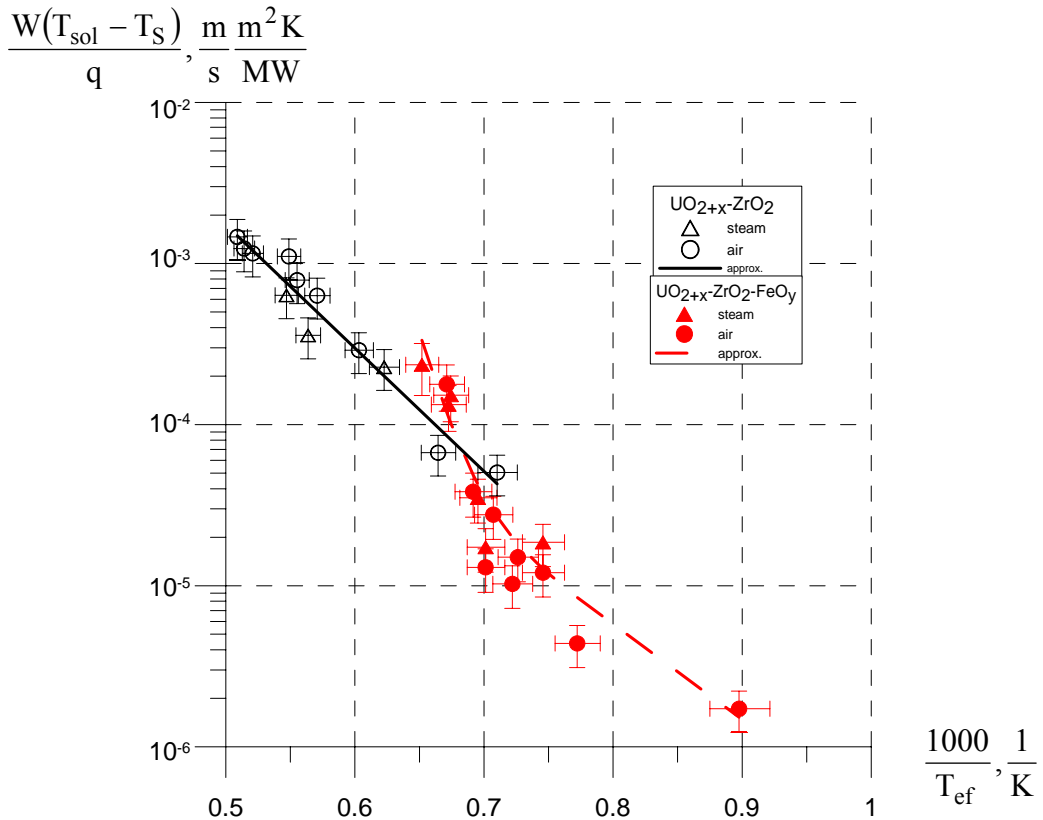


Fig. 3.5 – Experimental data generalization using T_{ef}

For the $UO_{2+x}-ZrO_2$ corium:

$$\frac{W(2723 - T_S)}{q} = 11.6 \exp\left(-\frac{1.46 \cdot 10^5}{RT_{ef}}\right). \tag{18}$$

For the $\text{UO}_{2+x}\text{-ZrO}_2\text{-FeO}_y$ corium:

$$\frac{W(1613 - T_S)}{q} = 0.28 \exp\left(-\frac{1.12 \cdot 10^5}{RT_{\text{ef}}}\right) + 2 \cdot 10^{14} \exp\left(-\frac{5.24 \cdot 10^5}{RT_{\text{ef}}}\right). \quad (19)$$

It should be noted that correlations (18), (19) have been used iterationally to calculate T_{ef} and the activation energy.

The obtained values of activation energy indirectly characterize the process of Fe ions diffusion in the corium crust. For the $\text{UO}_{2+x}\text{-ZrO}_2$ corium, $E_a = 1.46 \cdot 10^5$ J/mol., while for the solid crust of the $\text{UO}_{2+x}\text{-ZrO}_2\text{-FeO}_y$ corium $E_a = 1.12 \cdot 10^5$ J/mol.

The ranges of correlations (16)-(19) application are determined by the ranges in which the decisive parameters change in the tests, in particular:

- for the $\text{UO}_{2+x}\text{-ZrO}_2$ corium, mass concentration of FeO_y in the melt falls within the 0 to 5% range, U/Zr atomic ratio is approximately 1.1, $T_S = 870 \dots 1370$ °C, $q = 0.74 \dots 1.19$ MW/m².
- for the $\text{UO}_{2+x}\text{-ZrO}_2\text{-FeO}_y$ corium, mass concentration of FeO_y in the melt falls within the 20 to 30%, U/Zr atomic ratio is 0.11...1.05, $T_S = 720\text{-}1200$ °C, $q = 0.3\text{-}1.3$ MW/m².

Reliability of the obtained correlations may be judged by the values of standard deviations for the experimental points, which are 25% for the $\text{UO}_{2+x}\text{-ZrO}_2$ corium and 35 % for the $\text{UO}_{2+x}\text{-ZrO}_2\text{-FeO}_y$ corium.

At the same time, it is necessary to mention another possible unaccounted inaccuracy, which is due to the fact that at some experimental points corrosion was occurring during the unsteady diffusion regime. This could lead to overrating the corrosion rate in comparison with its rate during the established regime (under the established distribution of concentrations of diffusing components in the corium crust). The said inaccuracy may lead to overrating the rate of corrosion slightly when using the obtained correlations, which are conservative, from this point of view.

Vagueness of the T_{sol} value in the tests with molten $\text{UO}_{2+x}\text{-ZrO}_2$ should be specially mentioned. At the initial stages of MC10 and MCP-2 Fe oxides were missing in the melt and $T_{\text{sol}} = 2450$ °C. However, the melt was growing richer in iron oxides as corrosion of steel was going on, and by the end of MC10 concentration of Fe was approximately 2 mass % [1], while in the end of MCP-2 it was 5 mass % (see Section 2.2.4). Though even the maximum attained concentration of Fe is apparently smaller than the amount that would correspond to the ultimate solubility of FeO_y in the ternary oxidic system in question, still T_{sol} is decreasing as the concentration of Fe keeps growing. The absence of necessary data about the considered conditions prevents evaluation of T_{sol} value for most experimental points in MC10 and MCP-2, thus augmenting inaccuracy of correlation (18) for the $\text{UO}_{2+x}\text{-ZrO}_2$ corium.

In conformity with successive T_S growth from one regime to another in MC10 and MCP-2, and with the increasing FeO_y concentration in the melt, the use of true T_{sol} values would have resulted in a smaller slope of the generalizing straight line in Fig. 3.5, i.e., in a smaller activation energy in (18) (with reduction of the preexponential factor) with a value approaching $1.12 \cdot 10^5$ J/mol. (the first item in the right part of (19)). At the same time, position of the extreme right point on the generalizing straight line in Fig. 3.5 will keep practically the same.

Therefore, it can be concluded that the value of the activation energy which characterizes the process of Fe^{2+} diffusion is weakly sensitive to changes in FeO_y concentration in the solid crust of the $\text{UO}_{2+x}\text{-ZrO}_2\text{-FeO}_y$ corium and is close to the corresponding value of Fe^{2+} diffusion in Fe_{1-x}O .

A comparison of the generalizing dependences for $\text{UO}_{2+x}\text{-ZrO}_2$ and $\text{UO}_{2+x}\text{-ZrO}_2\text{-FeO}_y$ in Fig. 3.5 in that temperature domain where T_{sol} of the $\text{UO}_{2+x}\text{-ZrO}_2\text{-FeO}_y$ corium crust still has not been attained, showed the $\text{UO}_{2+x}\text{-ZrO}_2$ corium corrosion rate (taking q and $T_{\text{sol}} - T_S$ normalization into account) to be higher than the iron oxides-containing corium corrosion rate. We believe this difference to be determined not so much by the difference in diffusion coefficients, as by the difference in Fe concentrations in molten coriums, due to which the

“diffusion pressure” is higher for $\text{UO}_{2+x}\text{-ZrO}_2$ than for $\text{UO}_{2+x}\text{-ZrO}_2\text{-FeO}_y$. Thus, the difference in the Fe^{2+} diffusion flows and, hence, in corrosion rates is provided.

3.4 The influence of the vessel steel corrosion at the interaction with corium on the IVR

The obtained correlations allow calculation of the reactor vessel walls thinning during melt retention on the bottom. Samples of such calculations, which employ the previously obtained correlations and are applicable in a limited range of T_S variation, are given in [10]. Since the rate of corrosion decreases abruptly following the decrease in the steel surface temperature (in the process of corrosion), it may be expected that corrosion of vessel steel presents no danger from the point of view of its influence on the vessel strength. The final verdict can be given after performing calculations for the high pressure scenario accident conditions, when the creep of steel is the main factor determining the vessel strength.

The results obtained for the $\text{UO}_{2+x}\text{-ZrO}_2\text{-FeO}_y$ corium, however, evidence that corrosion intensifies at $T_S > 1050^\circ\text{C}$ and may make it necessary to take thermal effects into account. Indeed, in accordance with correlation (19), the rate of corrosion tends to an infinite quantity when T_S approaches $T_{\text{sol}} = 1340^\circ\text{C}$ (1613 K). This result corresponds to the accepted process model, in which the diffusion resistance determining the rate of corrosion is provided by the corium crust, in which a liquid phase appears at $T_S \rightarrow T_{\text{sol}}$, (according to experimental data, even earlier, already at 1050°C) in a quantity sufficient for the formation of liquid percolation clusters. It may be assumed that in reality the rate of corrosion will remain a finite quantity even in the absence of a solid corium crust on the steel surface, but its value may happen to be so big that calculations of the reactor vessel temperature condition will have to take the thermal effect of chemical reaction of steel oxidation into account. A sample calculation given in [1] shows that this effect leads to a local (in time) growth of the heat flux on the reactor vessel external surface cooled by boiling water.

Another potentially negative effect related to the corium crust liquefaction may be determined by an increased convective heat flux from molten corium to the vessel, which directly leads to an increase in heat flux on the reactor vessel external surface.

Obviously, all the above refers to the corium with low T_{sol} and big amounts of Fe oxides in its composition.

Though the discussed effects should be regarded as hypothetical at present, their influence on the IVR conditions may be of vital importance if they reveal themselves. Therefore, it seems practical to perform in future a test aimed at checking if the rapid steel corrosion may really take place and evaluating the associated thermal effects.

CONCLUSIONS

1. The MCP-2 has been performed and experimental data on the corrosion kinetics of VVER vessel steel at its interaction with molten $\text{UO}_{2+x}\text{-ZrO}_2$ corium have been obtained in air at 870...1370°C on the interface surface. The data from METCOR Project have been sufficiently supplemented.
2. The absence of influence of the oxidizing atmosphere composition (air, steam) on the kinetics of steel corrosion has been confirmed.
3. The combined experimental data and the results of posttest analyses for MCP-2 and other METCOR tests made it possible to develop a model of corrosion and obtain a correlations generalizing experimental data for the $\text{UO}_{2+x}\text{-ZrO}_2$ and $\text{UO}_{2+x}\text{-ZrO}_2\text{-FeO}_y$ coriums.
4. According to the accepted model, steel corrosion is controlled by diffusion in the corium crust on the steel surface. In the case with the $\text{UO}_{2+x}\text{-ZrO}_2\text{-FeO}_y$ corium with a relatively low T_{sol} , corrosion intensifies when the surface temperature (T_s) exceeds 1050°C, as a liquid phase forms in the corium crust. In the case with the $\text{UO}_{2+x}\text{-ZrO}_2$ corium with a high T_{sol} , no intensification of corrosion was observed up to the maximum T_s of 1370°C attained in the tests.
5. Taking into account the observed rapid growth of the corrosion rate at steel heating above 1050°C in the tests with the $\text{UO}_{2+x}\text{-ZrO}_2\text{-FeO}_y$ corium, it is proposed to perform a test aimed at evaluating thermal effects determined by the rapid oxidation of steel.

REFERENCES

1. Investigation of corium melt interaction with NPP reactor vessel steel (METCOR 2). Final technical report for the Project. 2006.
2. Investigation of molten $UO_2+x-ZrO_2-FeO_y$ corium interaction with NPP reactor vessel steel in the oxidizing atmosphere above the melt. MC12/07 test. 2007.
3. Markov V. K. et al. Uranium. Methods of its determination. Moscow, Atomizdat Publishers, 1964. (Rus.)
4. Riabchikov D.I., Seniavin M.M. Analytical chemistry of uranium. Moscow, Publishing House of the USSR Academy of Sciences. 1962. (Rus.)
5. Lukianov V.F., Savin S.B., Nikolskaya I.V. Photometric detection of uranium microquantities using reagent arsenazo III. JCh., v. XV, issue 3. 1960. (Rus.)
6. GOST 12365-84. Alloy and high-alloy steels. Methods of zirconium determination.
7. Yelinson S.V., Nezhnova T.I. Photometric determination of zirconium in niobium and other metals // Factory laboratory. Vol. 30, No.4, 1964.p. 396-399 (Rus.)
8. Goryushina V.G., Romanova E.V., Archakova T.A. Colorimetric methods of zirconium determination in alloys // Factory laboratory. Vol. 27, No.7, 1961. p. 795-797 (Rus.)
9. Tamman G., 1920. Uber Anlauffarben von Metallen. Z. Anorg. allg. Chem. B. III. H 1.5. 78-89.
10. S.V. Bechta, V.B. Khabensky et al. Corrosion of Vessel Steel during its Interaction with Molten Corium. Part 2: Model Development. NED. 236 (2006) 1362-1370.
11. S.V. Bechta, V.B. Khabensky et al. Corrosion of Vessel Steel during its Interaction with Molten Corium. Part 1: Experimental. NED. 236 (2006) 1810-1829.
12. Kofstad P., 1972. Nonstoichiometry. In: Diffusion and Electrical Conductivity in Binary Metal Oxides. Wiley-Interscience, New York.
13. Frost H.J., Ashby M.F., 1982. Deformation-Mechanism Maps. Pergamon Press, Oxford, New York, Toronto, Sydney, Paris, Frankfurt.